



2

David Taylor Research Center

Bethesda, MD 20084-5000

DTRC/SHD-1355-03 January 1992

Ship Hydromechanics Department

Departmental Report

**Turbulence at the Stern of an
Axisymmetric Model With and Without
Removable Appendages**

by

N.C. Groves, C.W. Jiang and Y.N. Liu

DTRC/SHD-1355-03 Turbulence at the Stern of an Axisymmetric Model
With and Without Removable Appendages

DTIC
SELECTE
FEB 21 1992
S B D



Approved for public release; distribution is unlimited

92-04352



MAJOR DTRC TECHNICAL COMPONENTS

- CODE 011 DIRECTOR OF TECHNOLOGY, PLANS AND ASSESSMENT
 - 12 SYSTEMS DEPARTMENT
 - 14 SHIP ELECTROMAGNETIC SIGNATURES DEPARTMENT
 - 15 SHIP HYDROMECHANICS DEPARTMENT
 - 17 SHIP STRUCTURES AND PROTECTION DEPARTMENT
 - 19 SHIP ACOUSTICS DEPARTMENT
 - 27 PROPULSION AND AUXILIARY SYSTEMS DEPARTMENT
 - 28 SHIP MATERIALS ENGINEERING DEPARTMENT

DTRC ISSUES THREE TYPES OF REPORTS:

1. **DTRC reports, a formal series**, contain information of permanent technical value. They carry a consecutive numerical identification regardless of their classification or the originating department.
2. **Departmental reports, a semiformal series**, contain information of a preliminary, temporary, or proprietary nature or of limited interest or significance. They carry a departmental alphanumeric identification.
3. **Technical memoranda, an informal series**, contain technical documentation of limited use and interest. They are primarily working papers intended for internal use. They carry an identifying number which indicates their type and the numerical code of the originating department. Any distribution outside DTRC must be approved by the head of the originating department on a case-by-case basis.

UNCLASSIFIED

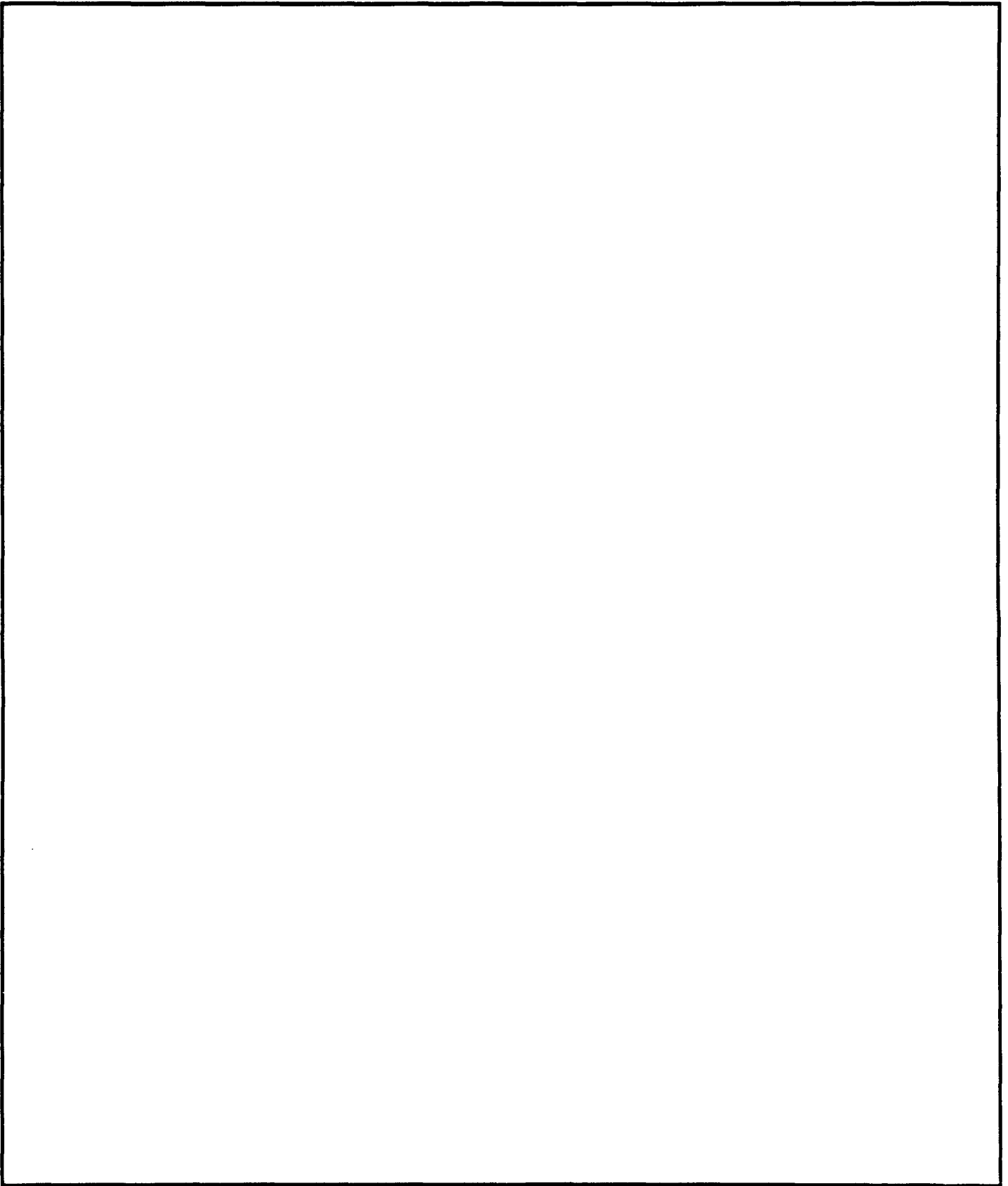
SECURITY CLASSIFICATION OF THIS PAGE

REPORT DOCUMENTATION PAGE

1a. REPORT SECURITY CLASSIFICATION UNCLASSIFIED			1b. RESTRICTIVE MARKINGS			
2a. SECURITY CLASSIFICATION AUTHORITY			3. DISTRIBUTION / AVAILABILITY OF REPORT Approved for public release; distribution is unlimited.			
2b. DECLASSIFICATION / DOWNGRADING SCHEDULE						
4. PERFORMING ORGANIZATION REPORT NUMBER(S) DTRC/SHD-1355-03			5. MONITORING ORGANIZATION REPORT NUMBER(S)			
6a. NAME OF PERFORMING ORGANIZATION David Taylor Research Center		6b. OFFICE SYMBOL <i>(if applicable)</i> Code 1542	7a. NAME OF MONITORING ORGANIZATION			
6c. ADDRESS <i>(City, State, and Zip Code)</i> Bethesda, MD 20084-5000			7b. ADDRESS <i>(City, State, and Zip Code)</i>			
8a. NAME OF FUNDING / SPONSORING ORGANIZATION Office of the Chief of Naval Research		8b. OFFICE SYMBOL <i>(if applicable)</i> ONR, Code 12	9. PROCUREMENT INSTRUMENT IDENTIFICATION NUMBER			
8c. ADDRESS <i>(City, State, and Zip Code)</i> Arlington, VA			10. SOURCE OF FUNDING NUMBERS			
			PROGRAM ELEMENT NO. 0101224N	PROJECT NO. R0092	TASK NO.	WORK UNIT ACCESSION NO. DN501370
11. TITLE <i>(Include Security Classification)</i> Turbulence at the Stern of an Axisymmetric Model With and Without Removable Appendages						
12. PERSONAL AUTHOR(S) Groves, Nancy C., Jiang, Chen-Wen, Liu, Yuan-Ning						
13a. TYPE OF REPORT Departmental		13b. TIME COVERED FROM _____ TO _____	14. DATE OF REPORT <i>(Year, Month, Day)</i> 1992 January		15. PAGE COUNT 43	
16. SUPPLEMENTARY NOTATION						
17. COSATI CODES			18. SUBJECT TERMS <i>(Continue on reverse if necessary and identify by block number)</i> turbulence ingestion axisymmetric hull removable appendages autocorrelation autospectrum			
FIELD	GROUP	SUB-GROUP				
19. ABSTRACT <i>(Continue on reverse if necessary and identify by block number)</i> The time-varying flow features of an axisymmetric model with removable appendages are studied. The random turbulence structure of the axial velocity component at an assumed propeller plane, but in the absence of a propeller, is examined through statistical techniques. Data are provided on the ingested turbulence for a three-dimensional axisymmetric geometry. The axial mean and axial fluctuating velocities are presented over the entire boundary layer region of the assumed propeller plane. The autocorrelation and power spectral density functions are presented at three radii and ten circumferential angles. The circumferential means of the axial integral length scales obtained from this model have been found to range from 10% to 15% of the maximum hull radius. In the absence of appendages, the largest values of this length scale occur near the hull boundary. In the presence of the appendages, the largest length scale occurs at the middle radius. At the outermost radius, roughly the maximum propeller radius, the integral length scale took on its smallest value. This value remained constant for all appendage configurations.						
20. DISTRIBUTION / AVAILABILITY OF ABSTRACT <input type="checkbox"/> UNCLASSIFIEDUNLIMITED <input checked="" type="checkbox"/> SAME AS RPT <input type="checkbox"/> DTIC USERS			21. ABSTRACT SECURITY CLASSIFICATION UNCLASSIFIED			
22a. NAME OF RESPONSIBLE INDIVIDUAL Nancy C. Groves			22b. TELEPHONE <i>(Include Area Code)</i> 202-227-1605		22c. OFFICE SYMBOL Code 1542	

UNCLASSIFIED

SECURITY CLASSIFICATION OF THIS PAGE



UNCLASSIFIED

SECURITY CLASSIFICATION OF THIS PAGE

CONTENTS

	Page
ABSTRACT.....	1
ADMINISTRATIVE INFORMATION.....	1
INTRODUCTION.....	1
VELOCITY MEASUREMENTS.....	3
STATISTICAL ANALYSIS.....	4
TURBULENCE INGESTION RESULTS.....	5
EXAMPLE APPLICATION.....	8
CONCLUSIONS.....	9
ACKNOWLEDGMENTS.....	10
REFERENCES.....	43

FIGURES

1. Schematic of model in DTRC AFF test section.....	11
2. Single element probe rake at $x/L=0.978$	12
3. SUBOFF model configurations.....	13
4. Measured axial mean velocity and turbulence intensity profiles at $x/L=0.978$ for three angular locations.....	14
5. Measured axial mean velocity at $x/L=0.978$ for three radial locations.....	15
6. Measured axial velocity fluctuations at $x/L=0.978$ for three radial locations.....	18
7. Normalized correlation function for three radii at $x/L=0.978$ for four hull configurations and ten angular locations.....	21
8. Axial integral length scales Λ (inches) at $x/L=0.978$ derived from hot-wire measurements.....	26
9. Spectral density function for bare hull at $x/L=0.978$ for ten angles and three radii.....	27
10. Spectral density function for hull with fairwater at $x/L=0.978$ for ten angles and three radii.....	30

FIGURES (Continued)

Page

11. Spectral density function for hull with four identical stern appendages at $x/L=0.978$ for ten angles and three radii33

12. Spectral density function for hull with fairwater and four identical stern appendages at $x/L=0.978$ for ten angles and three radii36

13. Comparison of experimental and analytical correlation functions for bare hull at $x/L=0.978$39

14. Fourier transform of three analytical correlation functions40

15. Experimental turbulence spectrum at $x/L=0.978$ for bare hull at $\theta=0^\circ$ 41

16. Comparison of experimental and theoretical transverse correlation for bare hull at $x/L=0.978$42

TABLE

1. Computed longitudinal integral length scale Λ as percentage of maximum hull radius $R_{max}=10$ in. (25.4 cm) at $x/L=0.978$ of the DARPA SUBOFF model..... 7

Accession For	
NTIS GRA&I	<input checked="" type="checkbox"/>
DTIC TAB	<input type="checkbox"/>
Unannounced	<input type="checkbox"/>
Justification _____	
By _____	
Distribution# _____	
Availability Codes	
Dist	Avail and/or Special
A-1	



ABSTRACT

The time-varying flow features of an axisymmetric model with removable appendages are studied. The random turbulence structure of the axial velocity component at an assumed propeller plane, but in the absence of a propeller, is examined through statistical techniques. Data are provided on the ingested turbulence for a three-dimensional axisymmetric geometry. The axial mean and axial fluctuating velocities are presented over the entire boundary layer region of the assumed propeller plane. The autocorrelation and power spectral density functions are presented at three radii and ten circumferential angles. The circumferential means of the axial integral length scales obtained from this model have been found to range from 10% to 15% of the maximum hull radius. In the absence of appendages, the largest values of this length scale occur near the hull boundary. In the presence of the appendages, the largest length scale occurs at the middle radius. At the outermost radius, roughly the maximum propeller radius, the integral length scale took on its smallest value. This value remained constant for all appendage configurations.

ADMINISTRATIVE INFORMATION

This work was performed at the David Taylor Research Center (DTRC) in Bethesda, Maryland 20884-5000 with work unit 1-1904-301, with funding from the Office of the Chief of Naval Research, element 0101224N.

INTRODUCTION

Important narrowband and broadband components of unsteady forces are generated by marine vehicle propulsors. Sources of unsteady broadband forces include propulsor cavitation, trailing edge vortex shedding, and turbulence ingestion.

Propeller blades passing through a non-uniform velocity field experience unsteady loads. Broadband forces result from the unsteady, nondeterministic loading of propeller blades. The low-frequency random loads are largely generated by the interaction of the blade with the inflow turbulence. The turbulence in the inflow to the propeller is called ingested turbulence.

Predictions of the propeller broadband thrust spectrum^{1,2,3} depend on propeller geometry and operating parameters, including blade radius, blade number, ship speed and propeller rpm. Predictions are further characterized by the turbulent structure of the inflow field, relying directly on the integral length scale of turbulence. Throughout the theoretical thrust spectrum calculation, the turbulence is assumed to be isotropic and, therefore, is characterized by exponential decay in the longitudinal correlation. While this approximation may be justified for grid-generated turbulence, it is unlikely to be justified for full-scale wake turbulence.

The measured characteristics of boundary layer turbulence generated by a model of an axisymmetric hull with removable appendages are studied in this report. The data provide an opportunity to examine the ingested turbulence for an axisymmetrical hull geometry. At the propeller plane, the hull boundary layer thickness is on the same order of magnitude as the propeller radius. Therefore, the propeller operates inside the turbulent hull boundary layer and is subjected to the random nature of turbulence. The experiments which are analyzed in this report were conducted in a low-turbulence wind tunnel where the free-stream turbulence level is much smaller than the boundary layer turbulence level. This assures that the turbulence characteristics investigated are generated by the hull boundary layer.

Numerous researchers have studied the physical mechanism of broadband force. Experimental and theoretical investigations show that turbulence is an important source mechanism for low frequency broadband force. Brooks and Schlinker⁴ have summarized the research on helicopter rotor broadband noise. Their paper chronicles both experimental and theoretical studies on turbulence ingestion, and links the turbulence statistics with the far-field spectrum of radiated noise.

More recent experiments by Aravamudan and Harris⁵ and Humbad and Harris⁶ have examined noise radiated from model helicopter rotors in an open-jet acoustic wind tunnel. Turbulence generation was controlled by grids mounted in the upstream section of the tunnel. Both turbulence and acoustic data were measured and prediction schemes were formulated to relate the two. These prediction schemes model isotropic turbulence and contain the integral turbulence length scale. These studies found the turbulence spectrum to follow the von Karman spectrum⁷, including a $-5/3$ power fall-off at high frequency.

Sevik¹ measured and predicted the unsteady thrust generated by a 10-bladed rotor subjected to free-stream grid-generated turbulence in a water tunnel. The measured spectrum was characterized by a series of humps which decreased in amplitude with increasing frequency. The theoretical predictions were based on isotropic turbulence and included as estimate of the integral length scale.

Recently, Martinez³ and Jiang, Chang and Liu² have extended Sevik's theory, which resulted in a considerable improvement in correlation with the experimental data. Martinez added the propeller rotational speed as a parameter into the correlation area. His results show small humps at blade rate frequencies which do not explain the near blade-rate humps in Sevik's experiment. Jiang, Chang, and Liu, who predict the broadband and near blade-rate humps simultaneously, show excellent agreement with the experimental spectra. Two critical components of the theoretical models of references 2 and 3 are the inflow turbulence and the transfer function between the turbulence intensity spectrum and the unsteady forces. All three applications consider the inflow to be isotropic and homogeneous.

The flow data analyzed in this report were measured at DTRC several years ago in a project termed SUBOFF^{8,9,*}. SUBOFF, sponsored by the Submarine Technology Program of the Defense Advanced Research Project Agency (DARPA), was designed to evaluate current computational fluid dynamics (CFD) capabilities. Simultaneous

* Huang, T.T. et al., "Measurements of Flows Over an Axisymmetric Body with Various Appendages in a Wind Tunnel," to be presented at the 19th ONR Symposium, Seoul, Korea, Aug. 1992.

experiments and CFD computations were performed of the stern flow field over a generic axisymmetric hull model with and without various appendages. Since the CFD predictions were made without prior knowledge of the actual experimental data, an assessment could be made of each code's design capabilities.

The scope of the SUBOFF experiments was extensive. Quantities measured include surface pressures and shear stress, pressure profiles, and mean velocity in the boundary layer and wake. The velocity data include axial, radial, and tangential time-average and root mean square fluctuating velocity components and axial-radial and axial-tangential Reynolds stresses. Selected axial mean and turbulence intensity velocity profiles measured at the propeller plane are included in this report.

Two types of velocity measurements are presented in this report. The axial mean and turbulence intensity velocities were measured using a three-component hot-film sensor. These data were sampled at a rate of 150 Hz for 5 seconds. The time-varying axial velocity components were measured at the propeller plane using a single-sensor hot film anemometer. These data were sampled at a rate of 20kHz for 30 seconds. Measurements were made using the single element sensor for four hull appendage configurations at three radii and ten azimuthal positions. These time-varying data are the basis of the present analysis of the characteristics of turbulence ingestion. Through statistical analysis of the axial component of velocity, an estimate is made of the longitudinal integral length scale.

In an example application, the normalized autocorrelation in the time domain, obtained from the measurements, is curve-fitted using two exponential functions and an inverse polynomial. The Fourier transform of these approximations represents the spectral density function of the measurements fairly well over the low to mid frequency range. There is some uncertainty in the spectra obtained from measurements for higher frequencies.

VELOCITY MEASUREMENTS

The velocity measurements were made several years ago under the SUBOFF project. Figure 1 is a schematic diagram of the generic model in the Anechoic Flow Facility (AFF) of the David Taylor Research Center (DTRC). As shown in Figure 1, the cylindrical coordinate system, with origin at the model nose, is adopted. X measures distance downstream, r measures radial distance, and θ measures angular distance. The angular position is defined positive clockwise with respect to the upright (12 o'clock) position, viewed from bow to stern.

The SUBOFF model has the following dimensions: overall length L of 4.36 m, forebody 1.02 m, parallel middle body 2.23 m, afterbody 1.11 m, and a maximum radius, R_{max} , of 0.25 m. Although no propeller was used in the experiment, measurements were made at an approximate propeller location of $x/L=0.978$. A removable fairwater of length 0.37 m is located at 0° with leading edge at $x/L=0.212$. Four identical stern appendages, also removable, are located with trailing edge at $x/L=0.920$ and with centerlines at 0° , 90° , 180° , and -90° .

Two struts support the model from below at $\theta=180^\circ$. These struts influence the mean flow over a $\pm 30^\circ$ envelope. Therefore, any measurement in the 150° to 210° range may be contaminated by strut effects.

All experiments were conducted at a Reynolds number, based on model length, of 1.2×10^7 . To assure turbulent flow, a trip wire was placed on the hull at 5% of the model length. The appendages were untripped.

At the assumed propeller location $x/L=0.978$, simultaneous time-varying velocity measurements were made at ten azimuthal locations. Measurements were taken using ten single sensor hot-film probes placed in a rake. The sensors were paired in the rake. Each of the sensors in a pair was separated by an 18° angular gap. Each sensor pair was separated by 54° . The rake provides for measurements at three radial locations, $r/R_{\max}=0.3, 0.4, \text{ and } 0.5$. At the test Reynolds number, the flow at all three radii was inside the boundary layer. A schematic of the probe rake and sensor arrangement is shown in Figure 2.

The accuracy of the hot-film measurements was addressed in Reference 10. The largest axial velocity uncertainty, $\pm 2.12\%$, was estimated to occur from the speed calibration. The repeatability of the axial velocity was estimated at $\pm 0.04\%$. The overall accuracy of the axial velocity was found to be $\pm 2.21\%$.

The single sensor probes were aligned to measure the axial component of the velocity. Data were sampled at a rate of 20 kHz for 30 seconds. The resulting 600,000 velocity measurements for each probe location were stored on a computer before the probes were moved to a different radial position in the wake.

Identical velocity measurements were made for four model configurations: bare hull, hull with fairwater, hull with four identical stern appendages, and hull with both fairwater and stern appendages. These configurations are summarized in Figure 3. Data for the bare hull serve as a basis on which to examine the flow effects due to the appendages.

STATISTICAL ANALYSIS

The measured axial velocity described in the preceding section is random in nature. This type of data is conveniently interpreted using statistical techniques to compute mean values, correlation functions, and spectral density functions. The axial component of mean velocity, denoted \bar{u}_x , is derived from the time data by

$$\bar{u}_x = \lim_{N \rightarrow \infty} \frac{1}{N} \sum_{j=1}^N u_x(t_j) \quad (1)$$

where N is the number of data samples and t_j is the time.

The axial component of the velocity fluctuations is given as

$$u'_x(t_j) = u_x(t_j) - \bar{u}_x \quad (2)$$

The turbulence properties relating to the broadband force may be described in terms of velocity correlations in time. The autocorrelation function relates the velocity received at

a measuring point at time t to the velocity received at the same point at a time delay $t_j+\tau$. The axial autocorrelation function, denoted R_{xx} , at time delay τ is given by

$$R_{xx}(\tau) = \lim_{N \rightarrow \infty} \frac{1}{N} \sum_{j=1}^N u'_x(t_j) u'_x(t_j+\tau) \quad (3a)$$

The axial integral length scale Λ , derived from the autocorrelation curve is

$$\Lambda = \frac{\overline{u_x}}{R_{xx}(0)} \int_0^{\infty} R_{xx}(\tau) d\tau \quad (3b)$$

Taylor's hypothesis of frozen convection¹¹ is assumed in this derivation. In this hypothesis, turbulence is regarded as a frozen pattern of eddies being swept past the observer at a fixed speed, i.e., the mean velocity $\overline{u_x}$.

The autospectral density function describes the general frequency composition of random data in terms of the spectral density of its mean square value. The spectral function is useful for determining the frequency range of the energy generated by the turbulence. Although this function is the Fourier transform of a correlation function, the SUBOFF spectra were obtained directly from the hot-film velocity measurements. The axial autospectrum, denoted S_{xx} is given by

$$S_{xx}(f) = \lim_{T \rightarrow \infty} \frac{1}{T} E[|X(f,T)|^2] \quad ,$$

where

$$|X(f,T)|^2 = \sum_{j=1}^N [u'_x(t_j)\cos 2\pi f t_j]^2 + \sum_{j=1}^N [u'_x(t_j)\sin 2\pi f t_j]^2 \quad (4)$$

TURBULENCE INGESTION RESULTS

The radial variation of the mean axial velocity and turbulence intensity measurements for each appendage configuration at three selected angular positions on the hull are shown in Figure 4. These data were measured using the three-element sensor and the 150 Hz sampling rate. The results indicate the fairwater and stern appendage effects at $\theta=0^\circ$, the stern appendage effects at $\theta=-90^\circ$, and the bare hull effects at $\theta=144^\circ$. As expected, the bare hull data, Figure 4a, collapse to a single curve. This collapse indicates that the model is properly aligned in the wind tunnel and that the hot-film system is working correctly.

The effect of the fairwater, represented by the profile at $\theta=0^\circ$, is clearly visible in Figure 4b. The two profiles away from the fairwater at $\theta=144^\circ$ and -90° closely resemble

the bare hull profiles. However, the fairwater creates a higher velocity near the hull wall and a lower velocity away from the wall when compared with the bare hull profiles.

The influence of the stern appendages is shown in Figure 4c. The two appendages at 0° and -90° create a much larger velocity near the hull. The velocity approaches the bare hull value near the edge of the boundary layer.

Finally, Figure 4d shows the influence of the individual appendages on the mean velocity. In the inner boundary layer region, the combination of fairwater and stern appendage produces a dramatic increase in velocity at $\theta=0^\circ$. A somewhat smaller but substantial velocity increase at -90° results from the stern appendages alone. In the outer boundary layer region, the velocity at 0° is slower than at either 144° or -90° . Comparison of Figure 4d with the 0° profiles in Figures 4b and 4c, reveals that the velocity decrease is caused by the fairwater.

The turbulence intensity distributions, also shown in Figure 4, are fairly similar for the different configurations and angular positions. The intensities are largest in value close to the hull surface and decay to almost zero before reaching the maximum hull radius.

Figures 5 and 6 present the circumferential variation of the mean velocity and turbulence intensity measurements at the three measurement radii, $r/R_{\max}=0.3, 0.4$ and 0.5 . In each of these figures, results for an appended hull configuration are compared with the bare hull. The data were measured in 1° to 2° increments using a three-element sensor at a sampling rate of 150 Hz. The dashed vertical lines, indicating the locations of the ten single-element time-varying measurement sensors, are for reference purposes only. The flow disturbance created by the support struts at $\theta = 180^\circ \pm 30^\circ$ is shown clearly in these figures. The velocity trends noted in Figure 4 are reinforced in Figures 5 and 6. For example, Figure 5a shows the higher velocity generated from the fairwater when compared to the bare hull. This difference in velocity rapidly dies out as the radius increases.

The autocorrelation functions, derived from the hot-film, time-varying measurements of the axial velocity, are shown in Figure 7. The ordinate has been normalized by the autocorrelation function at time delay $\tau=0$. The data for all four configurations are shown on a single graph. The graphs are grouped by increasing radius and paired by their placement in the probe rake.

The autocorrelation functions in Figure 7 exhibit several striking features. First, the degree of axial velocity correlation diminishes rapidly. For all the measurements, the correlation reaches a value of zero prior to 0.020 sec. This clearly illustrates the random nature of the turbulence in the boundary layer. Second, the correlation profiles display various degrees of similarity as the hull configuration is modified. For example, the correlations are quite similar for all geometries at the outermost radius, $r/R_{\max}=0.5$. An exception occurs at $\theta = -90^\circ$ where the velocities generated by the stern appendages are more uncorrelated than at the other angular positions. At $r/R_{\max}=0.3$, the innermost radius, greater variation in the correlation function exists than at the outermost radius. The correlation function at this innermost radius decreases rapidly for data within $\pm 18^\circ$ of a stern appendage, as illustrated at $-18^\circ, 0^\circ, 72^\circ, -90^\circ$, and -72° .

Figure 8 shows the computed values of the axial integral length scale for the various model hull configurations. The integral length scales range in value from 0.7 in. to 1.9 in. For the bare hull and hull with fairwater, the smallest length scales are approximately 1 in.

and occur at the outermost radius. For the configurations with stern appendages, the smallest length scale is 0.7 in. This value occurs at $\theta=-90^\circ$, which is the centerline of the stern appendage profile. For stern-appended configurations, there is little variation in the length scale with radial position at this angular position, indicating the presence of small eddies directly behind the appendage. This trend is also exhibited at $\theta=0^\circ$ for the hulls with appendages, i.e., fairwater and/or stern appendages.

With the exception of $\theta=126^\circ$, the largest values of Λ for the stern-appended hull occur at the middle radius $r/R_{max}=0.4$. This suggests that the largest eddies are concentrated at a radial distance of 4 inches (1.6 cm) from the model hull surface.

Table 1 gives the circumferential mean values of the integral length scales for the four hull configurations. Without the stern appendages, the larger length scales occur closest to the hull. With the stern appendages, the middle radius has the largest length scale. The radial means are also shown in Table 1. These radial mean values indicate that the fairwater has little effect on the integral length scale at the propeller plane. This may perhaps be a result of the large distance between the fairwater and the propeller plane. A slight reduction in the mean integral length scale occurs for stern-appended configurations.

Table 1. Computed longitudinal integral length scale Λ as percentage of maximum hull radius $R_{max}=10$ in. (25.4 cm) at $x/L=0.978$ of the DARPA SUBOFF model

r/R_{max}	Bare Hull	Hull with Fairwater	Hull with Stern Appendages	Hull with Fairwater & 4 Stern Appendages
0.3	15.1%	15.3%	11.4%	11.6%
0.4	13.8%	12.9%	14.8%	14.3%
0.5	10.4%	10.7%	10.4%	10.9%
Radial Average	13.1%	13.0%	12.2%	12.3%

The autospectral density functions are also derived directly from the measured hot film data. These functions are shown in Figures 9 through 12. Typically, the spectra contain three energy regions, each distinguished by a spectra with a unique slope. The largest energy is concentrated in the low frequency region, i.e., frequencies less than 100 Hz. The slope in this region approaches zero as the frequency approaches zero. As the distance from the hull surface increases, the energy in this region is seen to decrease. The region of zero slope extends to higher frequencies in the vicinity of the appendages. This is illustrated from the two stern appendage configurations. At the innermost radius, $r/R_{max}=0.3$, Figures 11a and 12a show the slope approaching zero for azimuthal angles closest to the appendages. These angles include 0° , 72° , -90° , and -18° . This indicates that the appendages create smaller eddies compared with the bare hull configuration.

The mid-frequency range for these data contains frequencies between roughly 100 and 1000 Hz. The spectra slopes in this region are approximately -1 for the bare hull and the hull with fairwater at all three radii. Under the influence of the stern appendages, the spectra slope flatten with increasing distance from the hull, shown at 0° and -90° .

Finally, the spectral densities in the high frequency range of these data, ≥ 1000 Hz, are fairly insensitive to changes in configuration and distance from the hull. The slope of all curves is approximately -4 which is greater than the -5/3 slope of grid generated turbulence. This region is also characterized by energy spikes. These spikes are not caused by turbulence but are an artifact resulting from the instrument resonance.

EXAMPLE APPLICATION

In this section three different equations are applied to represent the integral length scale Λ obtained from the SUBOFF measurements. In order to apply the AFF turbulence characteristics to various forward speeds and model lengths, the time scale in the correlation curves will be normalized to the time at which $R_{xx}(\tau)/R_{xx}(0) = 0.5$, denoted as $t_{0.5}$. In previous applications^{1,2,3}, turbulence correlation was assumed to be an exponential function, $R_{xx}(\tau)/R_{xx}(0) = e^{-\bar{u}_x \tau / \Lambda}$, where Λ is defined as the turbulence length scale. The exponential correlation function is shown in Hinze⁷ to be a good assumption for grid-generated turbulence, providing excellent agreement between measured and theoretical results for longitudinal (axial) and transverse correlations and spectral distribution.

In the current application, three curves are chosen to simulate the axial correlation behavior of the bare hull SUBOFF measurement data. Two curves are exponential of the form

$$R_{xx}(\tau)/R_{xx}(0) = e^{-\bar{u}_x \tau / \Lambda} \quad (5a)$$

where

$$\Lambda = - \frac{\bar{u}_x t_{0.5}}{\ln(0.5)} \quad (5b)$$

or

$$\Lambda = \frac{\bar{u}_x}{R_{xx}(0)} \int_0^{\infty} R_{xx}(\tau) d\tau \quad (5c)$$

The first approximation in Eqs. (5a) and (5b) passes through the data point at $t_{0.5}$. The second curve, using Eqs. (5a) and (5c) has the same area as the measured data curve. A third approximation, an inverse polynomial, is generated to match the bare hull experimental data at the innermost radius, $r/R_{max}=0.3$. This equation is:

$$R_{xx}(\tau)/R_{xx}(0) = \frac{1}{1+0.996(t/t_{0.5})+0.004(t/t_{0.5})^3} \quad (5d)$$

Figure 13 presents the comparison for the bare hull configuration of the experimental correlation results with the three equations provided above. The exponential curve matching the correlation area has been used in the propeller force calculation of Jiang, et al.². This curve is shown in Figure 13 to be a fairly good representation of the

correlation function at the outer radius. However, at the inner two radii, this curve fails to represent the experimental correlation for this set of data. Also, the curve-fit to the data at the radius $r/R_{max}=0.3$ does not match the experimental correlation at the outer two radii. These observations suggest that the turbulence measured on the SUBOFF model is a complicated phenomena which must be represented by some local flow properties. The effects of all three approximations on the propeller force calculation should be investigated.

The frequency and spectrum functions can be normalized using the mean velocity $\overline{u_x}$, the velocity fluctuations $\overline{u^2}$, and the displacement thickness δ^* . If the abscissa of the turbulent spectra are presented as $\omega\delta^*/\overline{u_x}$ and the ordinate as $S_{xx}(f)/\overline{u^2}$, the Fourier transform of these three correlation functions are given in Figure 14. Turbulence spectra measured in the AFF for the bare hull at $r/R_{max}=0.3, 0.4, \text{ and } 0.5$ at $\theta=0^\circ$ are furnished in Figure 15 for comparison. Figure 15 demonstrates that the turbulent spectra can be collapsed to a single curve at outer radii or at higher frequency under the proper normalization. The turbulence spectrum derived from the exponential match at $t_{0.5}$ provides a good description of the measured spectrum in the low frequency region containing the highest energy. However, the slopes differ significantly at higher frequencies. Here, the slope of the analytical curves approaches $-5/3$ whereas the slope of the SUBOFF experimental data is -4 . The causes of these differences are unclear at this time. One possible explanation is that the Reynolds number, $Re(\Lambda)$, for the laboratory test may be too small for the inertial subrange to be established. Tennekes and Lumley¹² show that the slope of the spectrum approaches -2 as the Reynolds number increases. It is expected that full-scale turbulence resulting from a higher Reynolds number would exhibit the inertial subrange and would follow the $\kappa^{-5/3}$ law. Also, the signal to noise ratio in this frequency range may be too low to provide meaningful turbulence spectra. This high frequency region contains a small fraction of the total turbulent energy and probably is not critical to full scale applications. Further study of this area is required to understand the physical phenomena.

Next, the theoretical transverse correlation is calculated based on the exponential longitudinal function using the assumption of isotropic and incompressible flow. The measured transverse correlation points are given in Figure 16 along with the theoretical curve. These measured results do not satisfy the isotropy condition assumed in theory. The measured data were taken at one fixed angular separation, namely 18° . Therefore, the anisotropy extent can not be fully determined from these limited results.

CONCLUSIONS

Through statistical analysis of mean and time varying velocity measurements, certain features of the turbulent flow generated at the propeller plane, in the absence of a propeller, by an axisymmetric model with removable appendages have been studied. The mean axial velocities and turbulence intensities clearly exhibit a three-dimensional nature in Figures 5 and 6. As expected, the flow disturbances are greatest near the hull surface and decay with increasing distance from the hull.

In the time domain, the autocorrelation functions of the axial velocity component in Figure 7 show a rapid decrease with separation time. This behavior illustrates the random nature of the turbulence in the boundary layer. The spectral analyses in Figures 9 through

12 show that the highest energy content of the axial velocities is in the frequency range less than 100 Hz. The circumferential average of the axial integral length scales computed from the autocorrelations, a measure of the turbulent eddies, range from 10% to 15% of the maximum hull radius. The fairwater was found to have little effect on the value of the integral length scale. Both the bare hull and the hull with fairwater configurations showed a decrease in integral length scale with increasing distance from the hull. The largest integral length scales for the stern-appended models occurred at the middle radius, suggesting additional flow mixing created by the presence of the stern appendages.

Finally, in an example application of these measurements, three analytic approximations were generated to a normalized, bare hull correlation function. Applying a Fourier transformation to these analytical representations yielded a frequency spectrum which closely matched the spectrum derived from the experimental data for frequencies less than about 1000 Hz. Above 1000 Hz, the analytically-derived spectrum approximated the $-5/3$ slope noted by previous researchers; the spectrum derived from measured data produces a slope of -4 . It is unclear if these differences result from actual physical phenomena or are simply shortcomings in the measurement data. The Reynolds number of the test may be too small for the inertial subrange to be established or the signal to noise ratio in this high frequency range may be too low to provide meaningful turbulence spectra.

Considering that the AFF-SUBOFF data were measured for CFD validation and never intended for turbulence ingestion analysis, the results of the present study have provided useful information into the turbulence characteristics of an axisymmetric body with appendages.

ACKNOWLEDGMENTS

In addition to the Office of the Chief of Naval Research who sponsored this work, the authors would like to express their gratitude to a number of other people who contributed to this project. We would like to thank Mr. Gary Jones of the Submarine Technology Program Office of DARPA for providing access to the SUBOFF data base and for providing computation facilities for performing the analysis. The staff of the DARPA Submarine Hydrodynamic/Hydroacoustic Technology Center were extremely helpful in setting up and storing the massive data base. In particular, we wish to thank Mr. Neil McElroy and Mr. Martin Burtness. The SUBOFF test engineers, including Dr. Han-Lieh Liu, Mr. James Blanton, Mr. Tom Forlini, and Mr. Scott Gowing, provided useful guidance into the test plan, the data acquisition and the data storage. Finally, we wish to thank Dr. Thomas Huang, Dr. Ming Chang and Dr. Han-Lieh Liu for their technical advice.

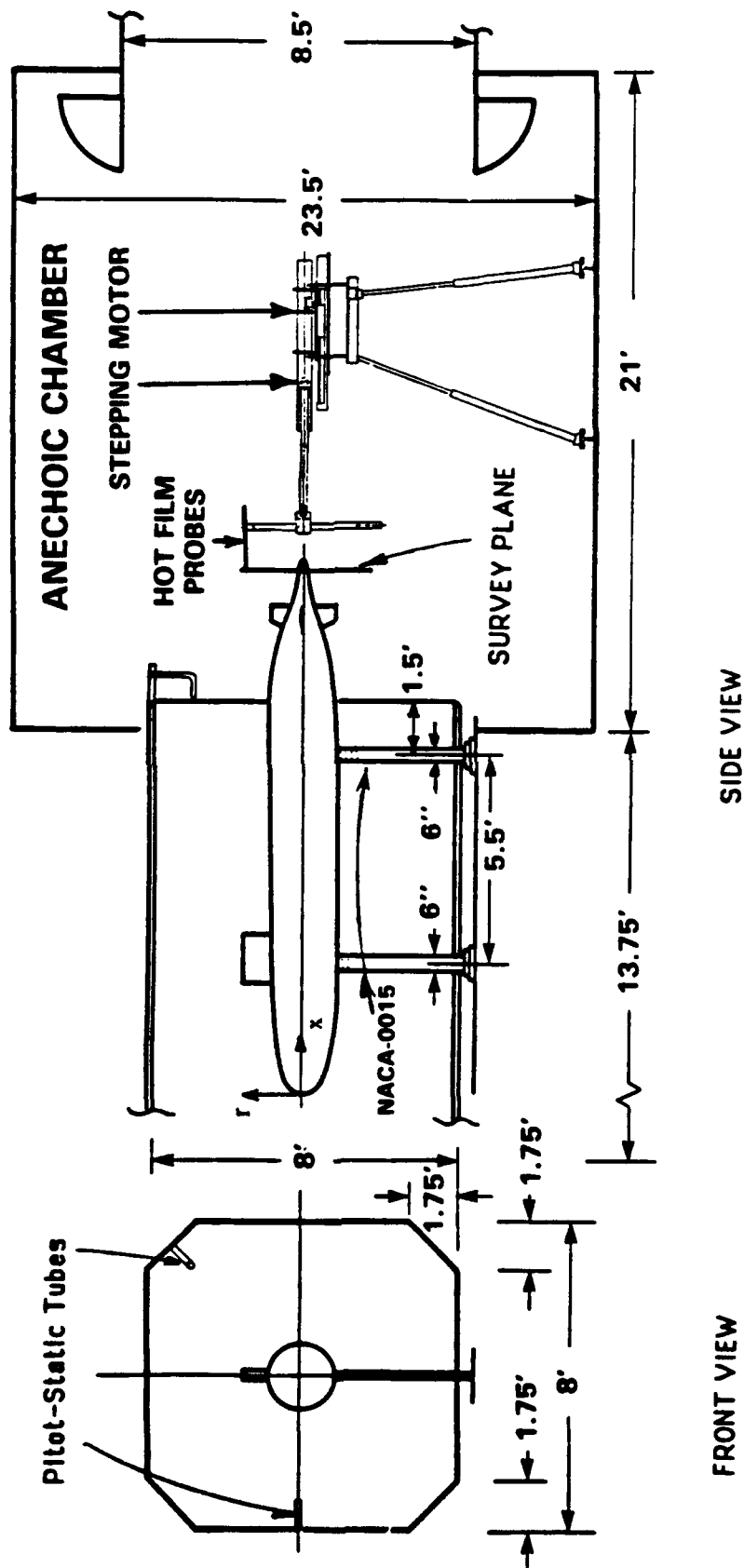


Fig. 1. Schematic of model in DTRC AFF test section.

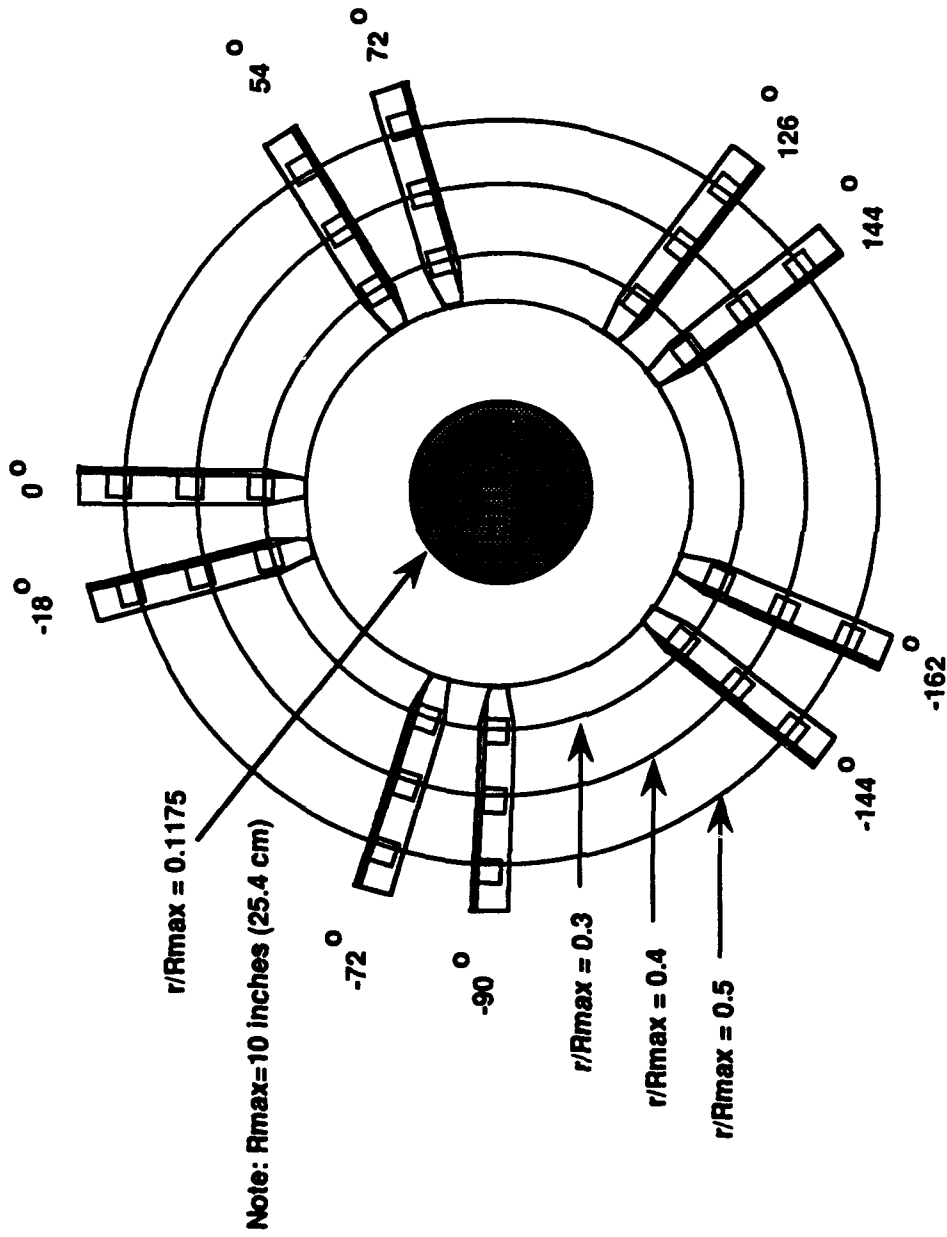
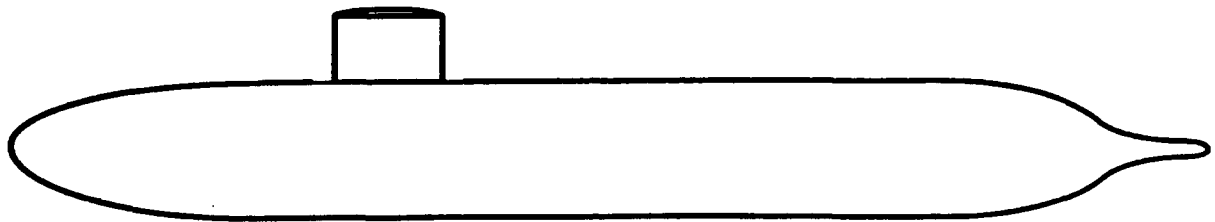


Fig. 2. Single element probe rake at $x/L=0.978$.



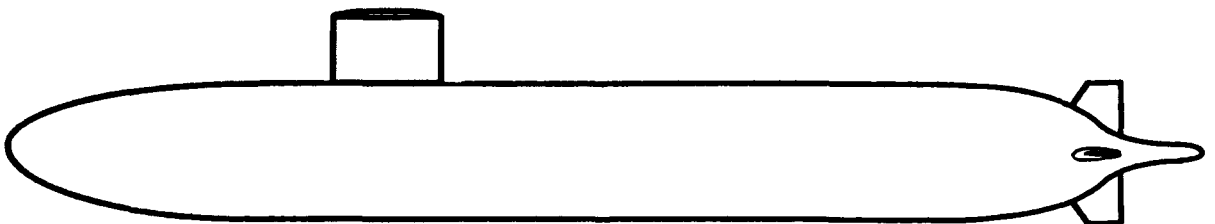
(a) Bare hull.



(b) Hull with fairwater.



(c) Hull with four identical stern appendages.



(d) Hull with fairwater and four identical stern appendages.

Fig. 3. SUBOFF model configurations.

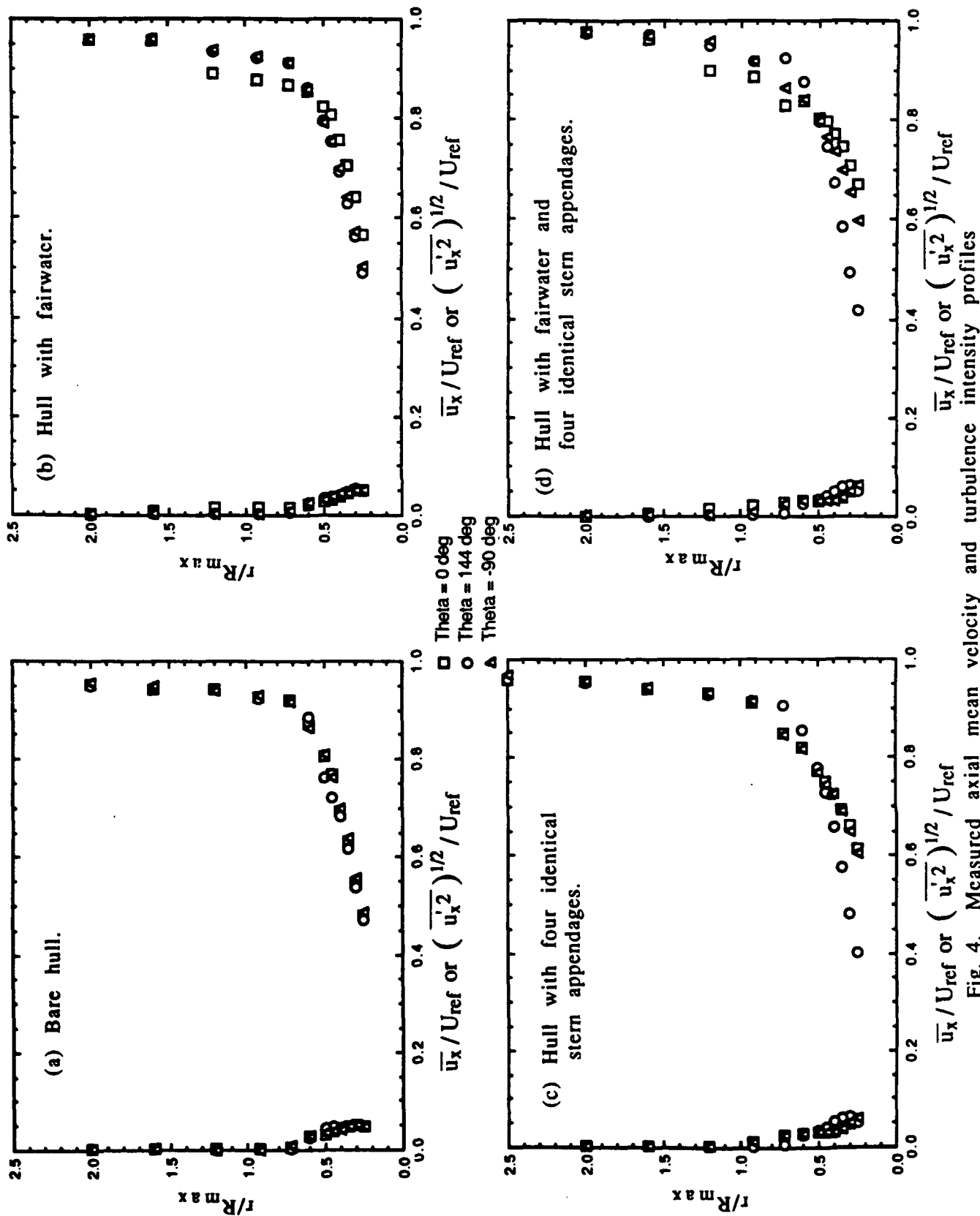


Fig. 4. Measured axial mean velocity and turbulence intensity profiles at $x/L=0.978$ for three angular locations.

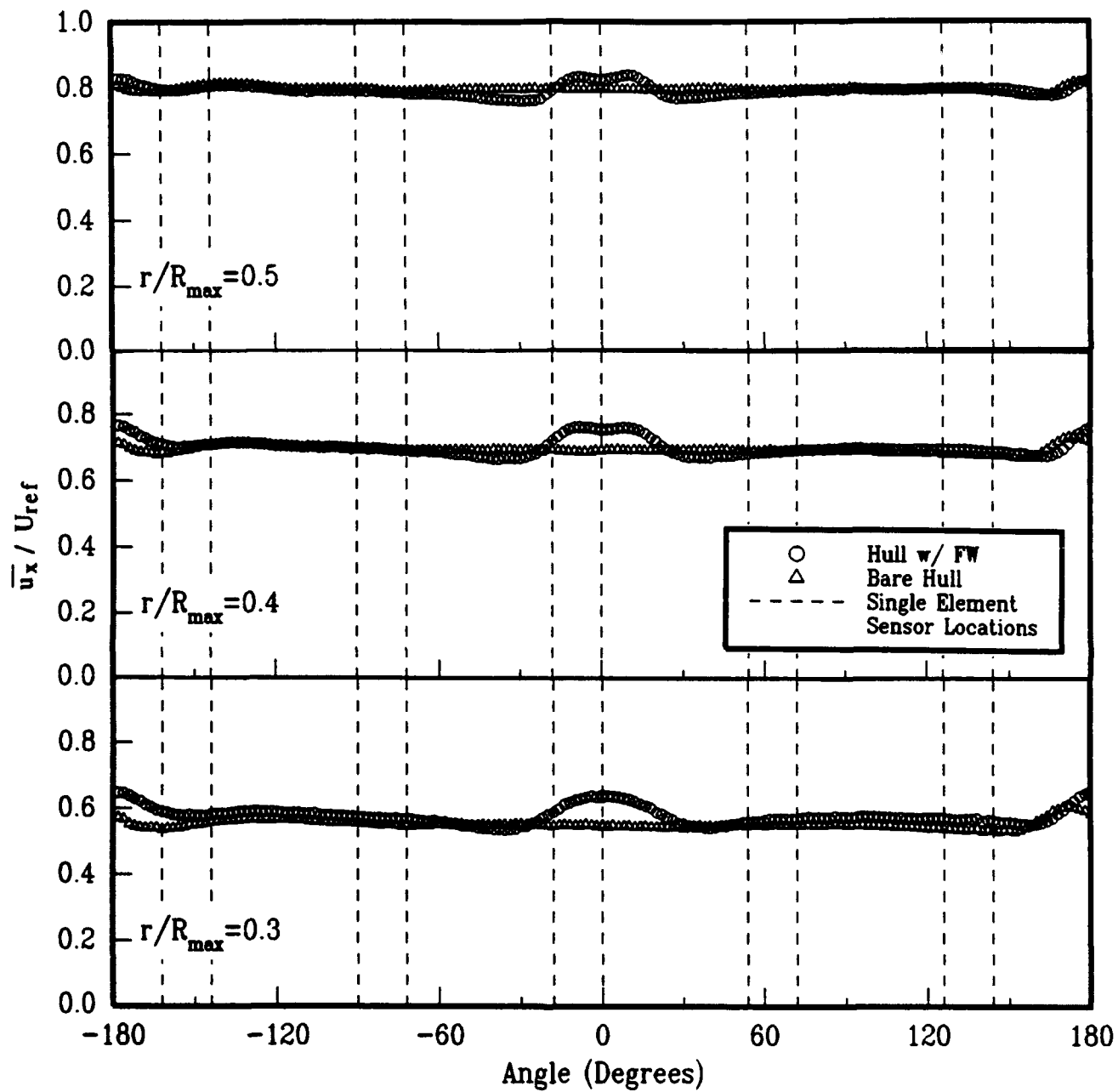


Fig. 5a. Bare hull versus hull with fairwater.

Fig. 5. Measured axial mean velocity at $x/L=0.978$ for three radial locations.

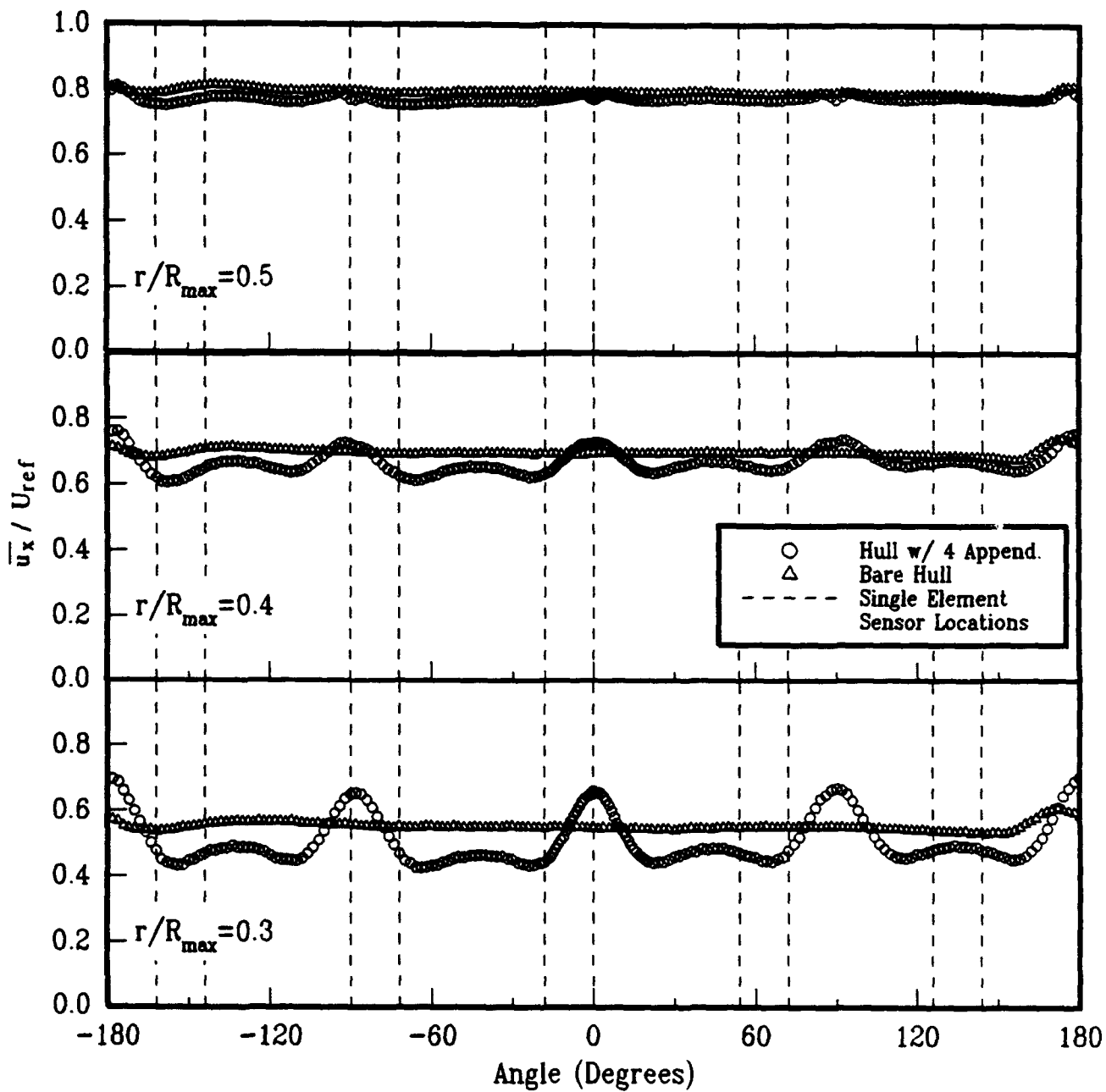


Fig. 5b. Bare hull versus hull with four identical stern appendages.

Fig. 5. (Continued)

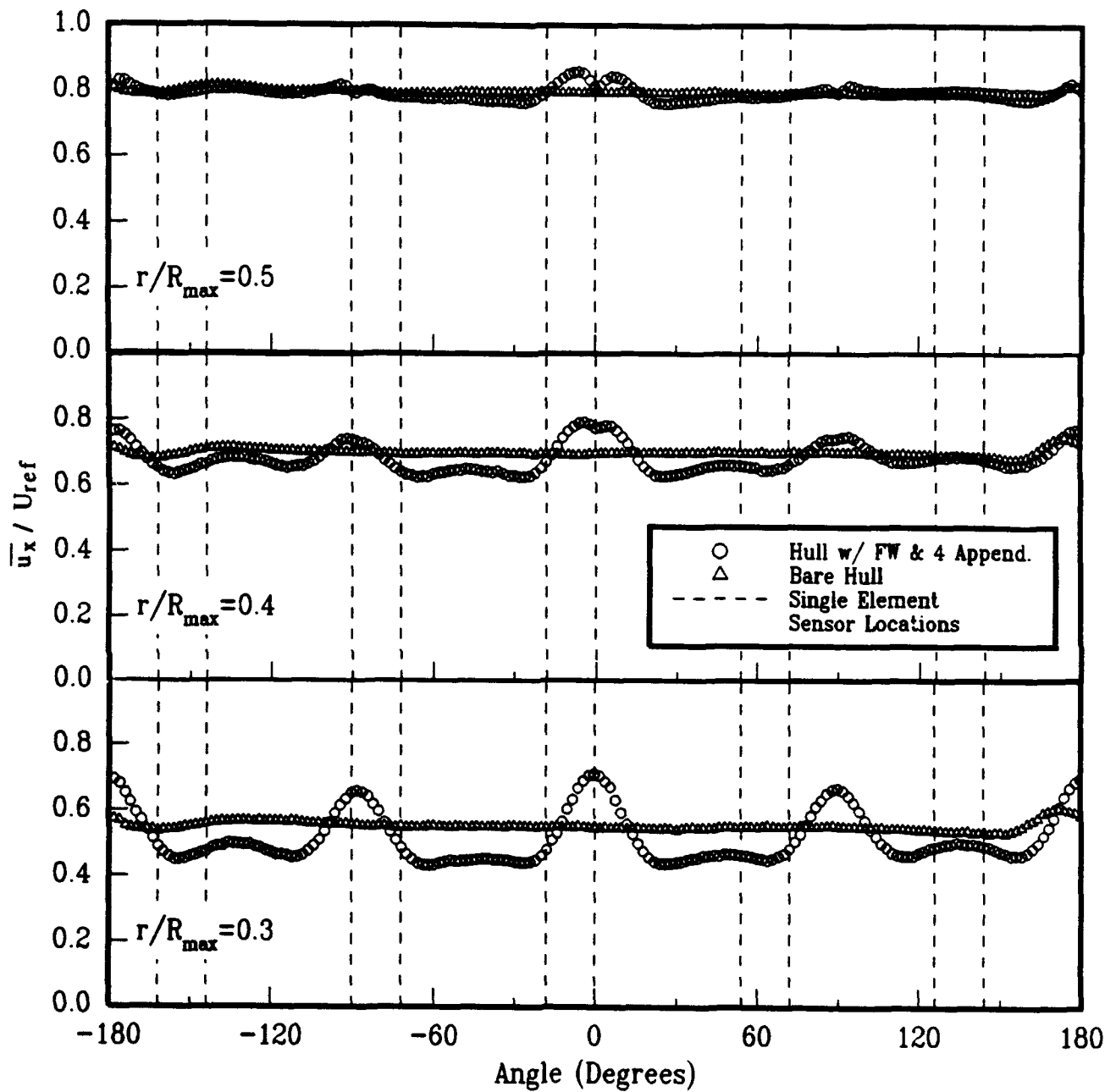


Fig. 5c. Bare hull versus hull with fairwater and four identical stern appendages.

Fig. 5. (Continued)

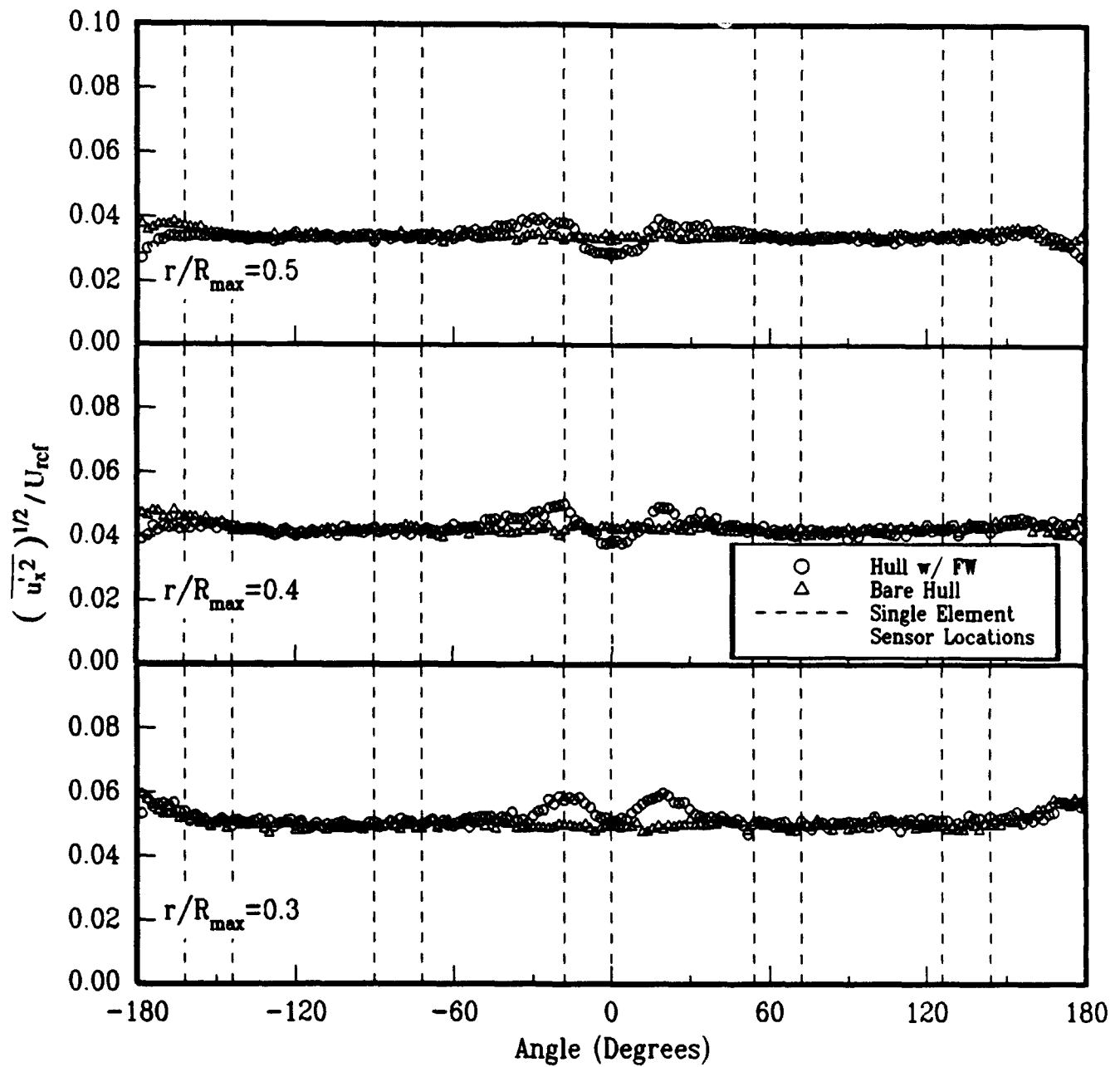


Fig. 6a. Bare hull versus hull with fairwater.

Fig. 6. Measured axial velocity fluctuations at $x/L=0.978$ for three radial locations.

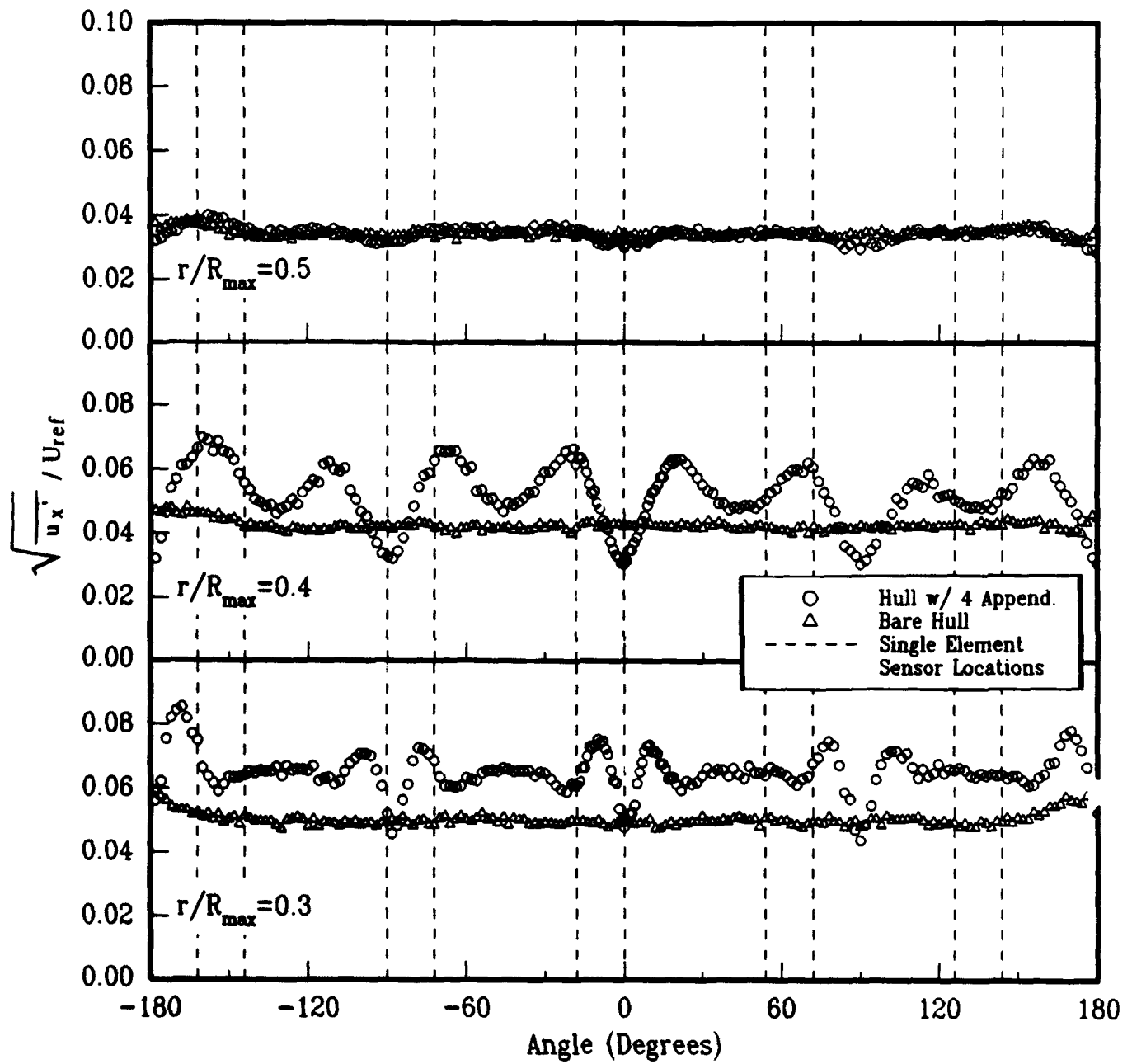


Fig. 6b. Bare hull versus hull with four identical stern appendages.

Fig. 6. (Continued)

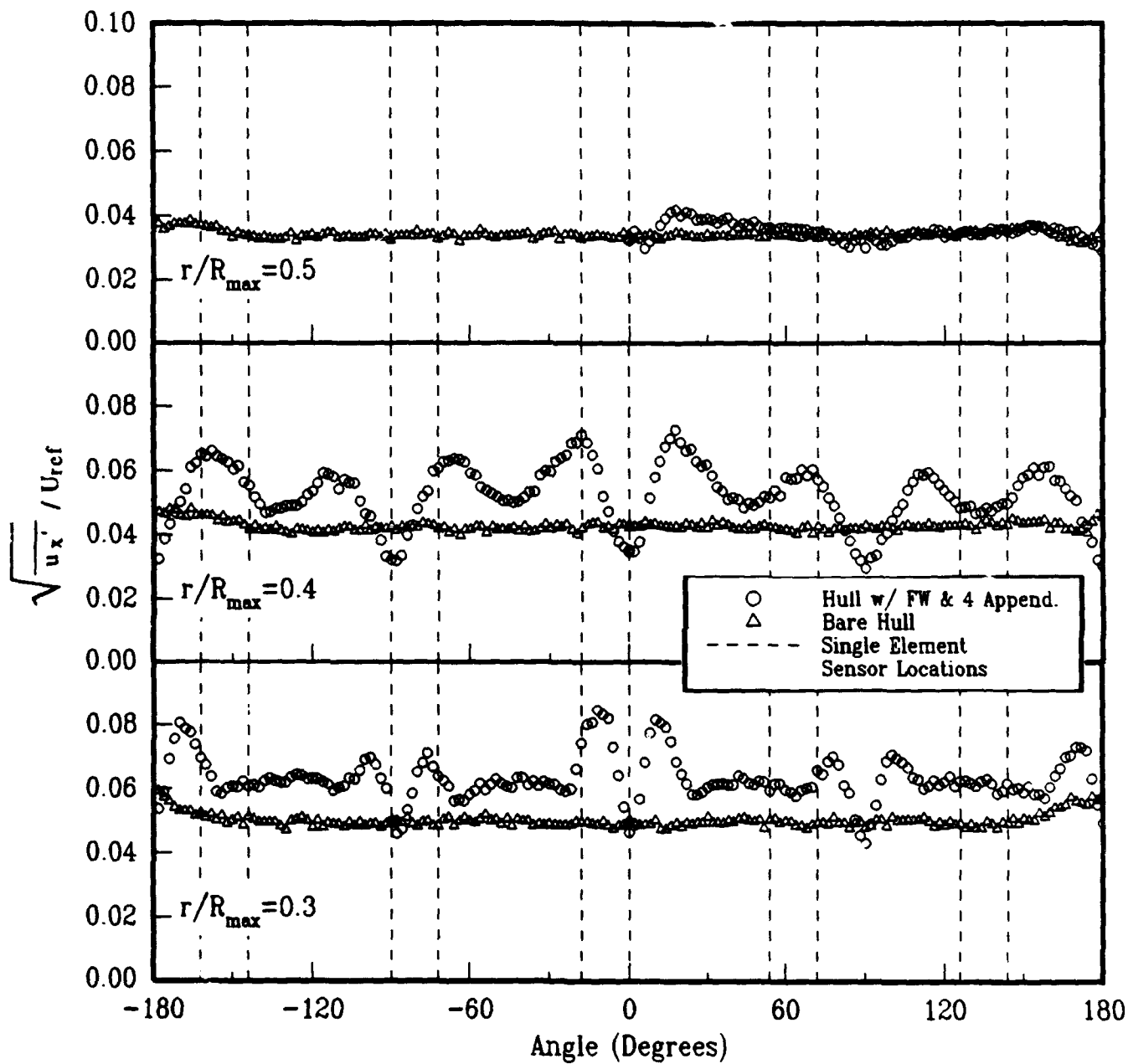


Fig. 6c. Bare hull versus hull with fairwater and four identical stern appendages.

Fig. 6. (Continued)

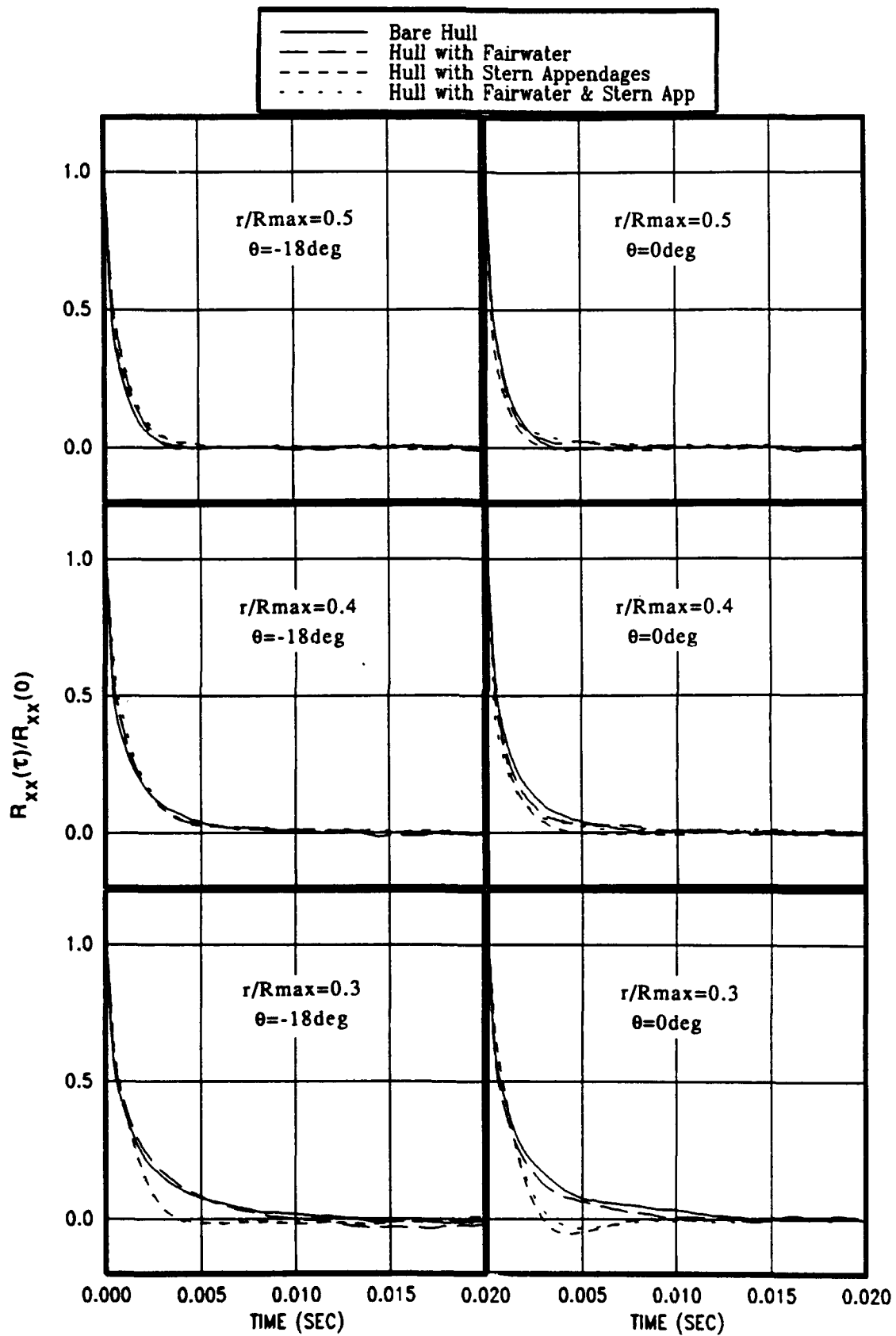


Fig. 7a. $\theta=-18^\circ$ and $\theta=0^\circ$.

Fig. 7. Normalized correlation function for three radii at $x/L=0.978$ for four hull configurations and ten angular locations

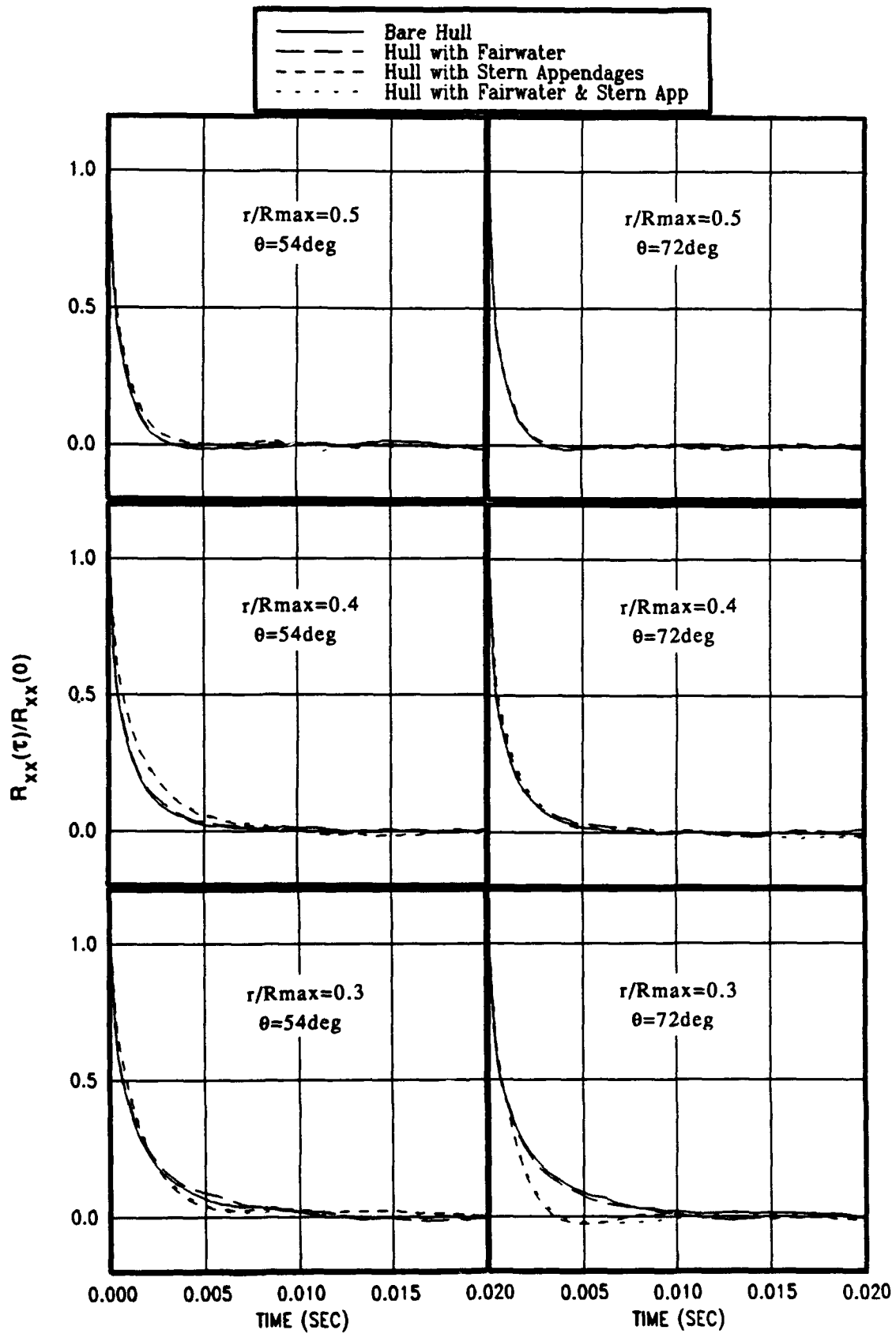


Fig. 7b. $\theta=54^\circ$ and $\theta=72^\circ$.

Fig. 7. (Continued)

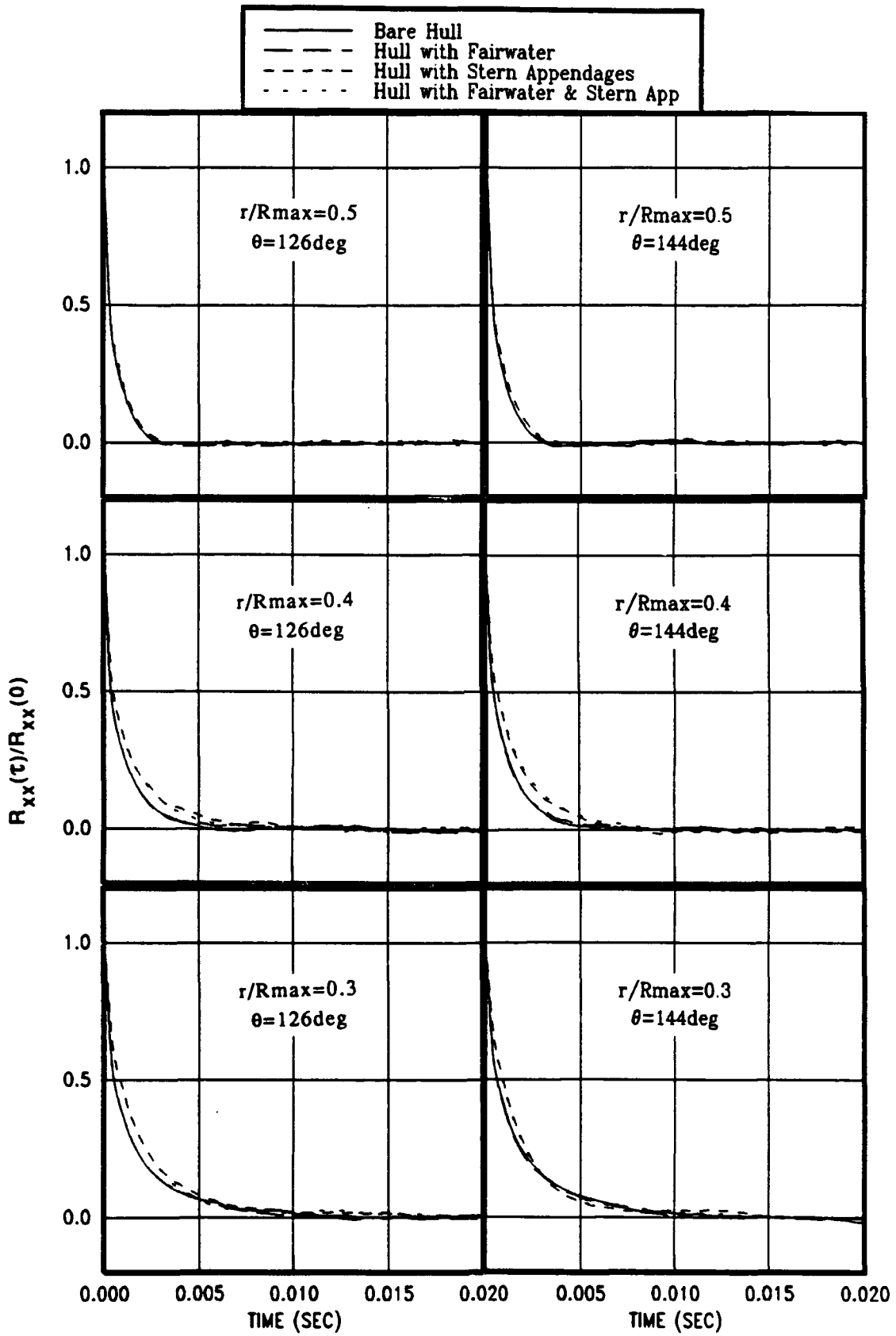


Fig. 7c. $\theta=126^\circ$ and $\theta=144^\circ$.

Fig. 7. (Continued)

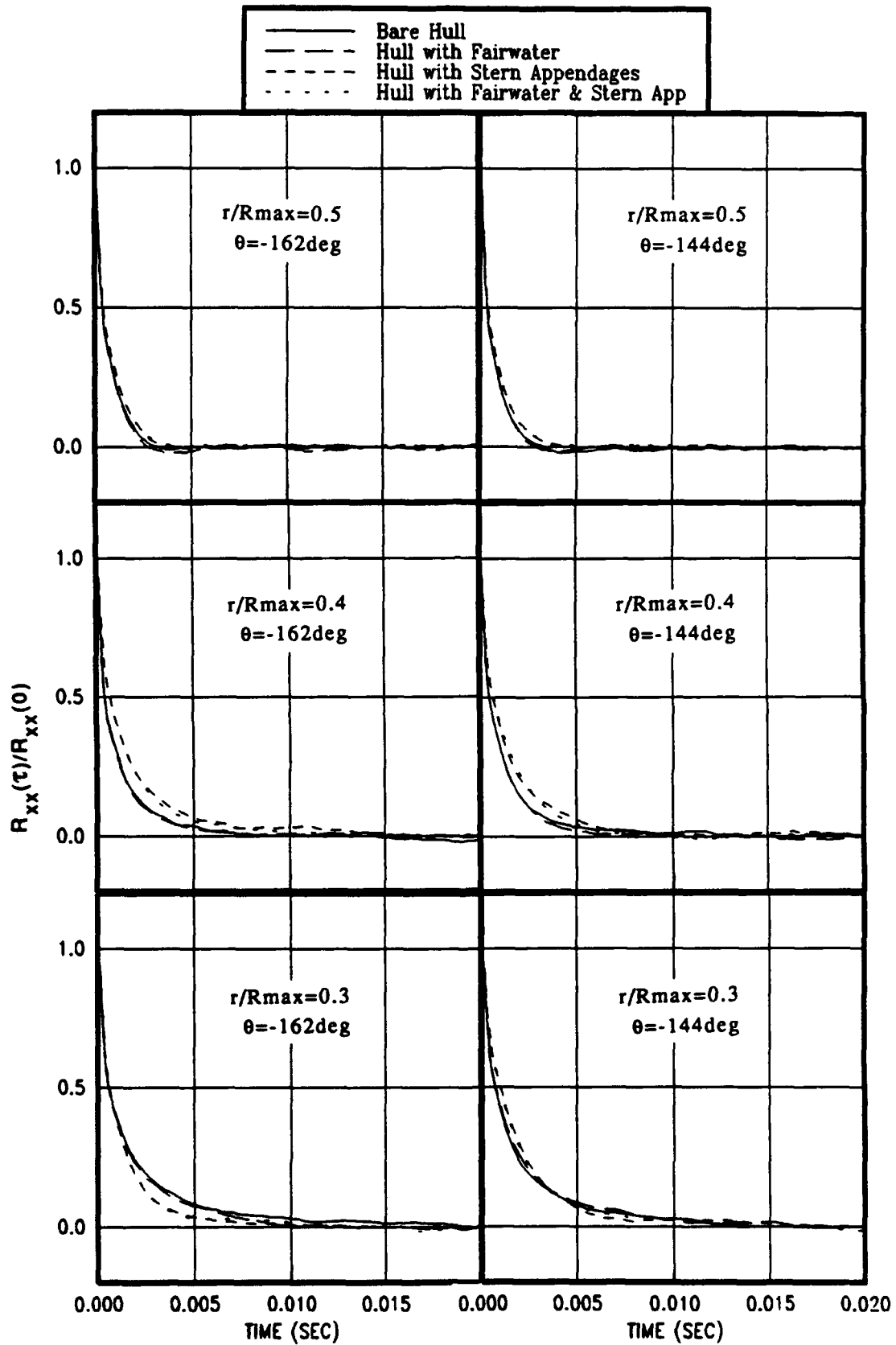


Fig. 7d. $\theta=-168^\circ$ and $\theta=-144^\circ$.

Fig. 7. (Continued)

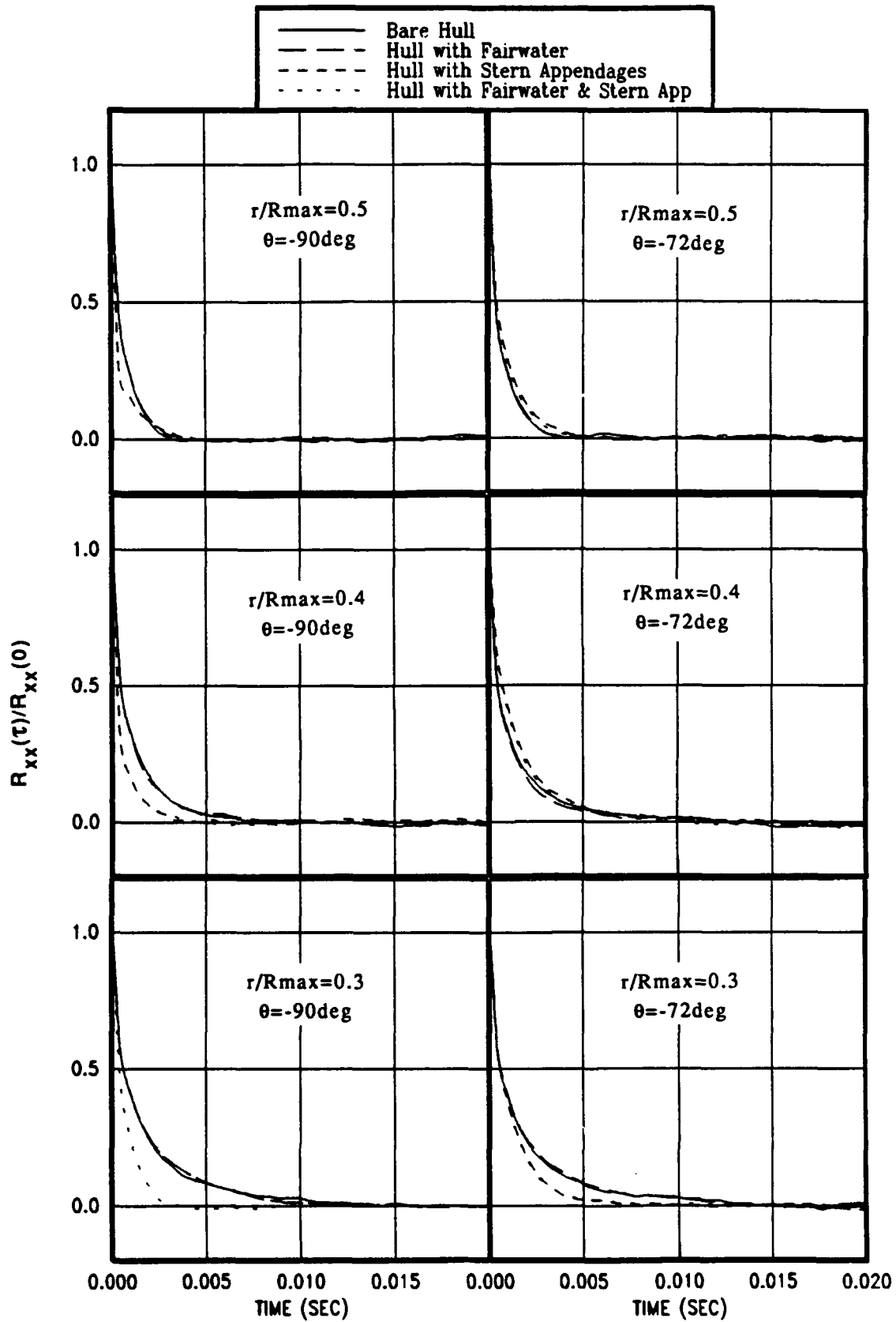


Fig. 7e. $\theta=-90^\circ$ and $\theta=-72^\circ$.

Fig. 7. (Continued)

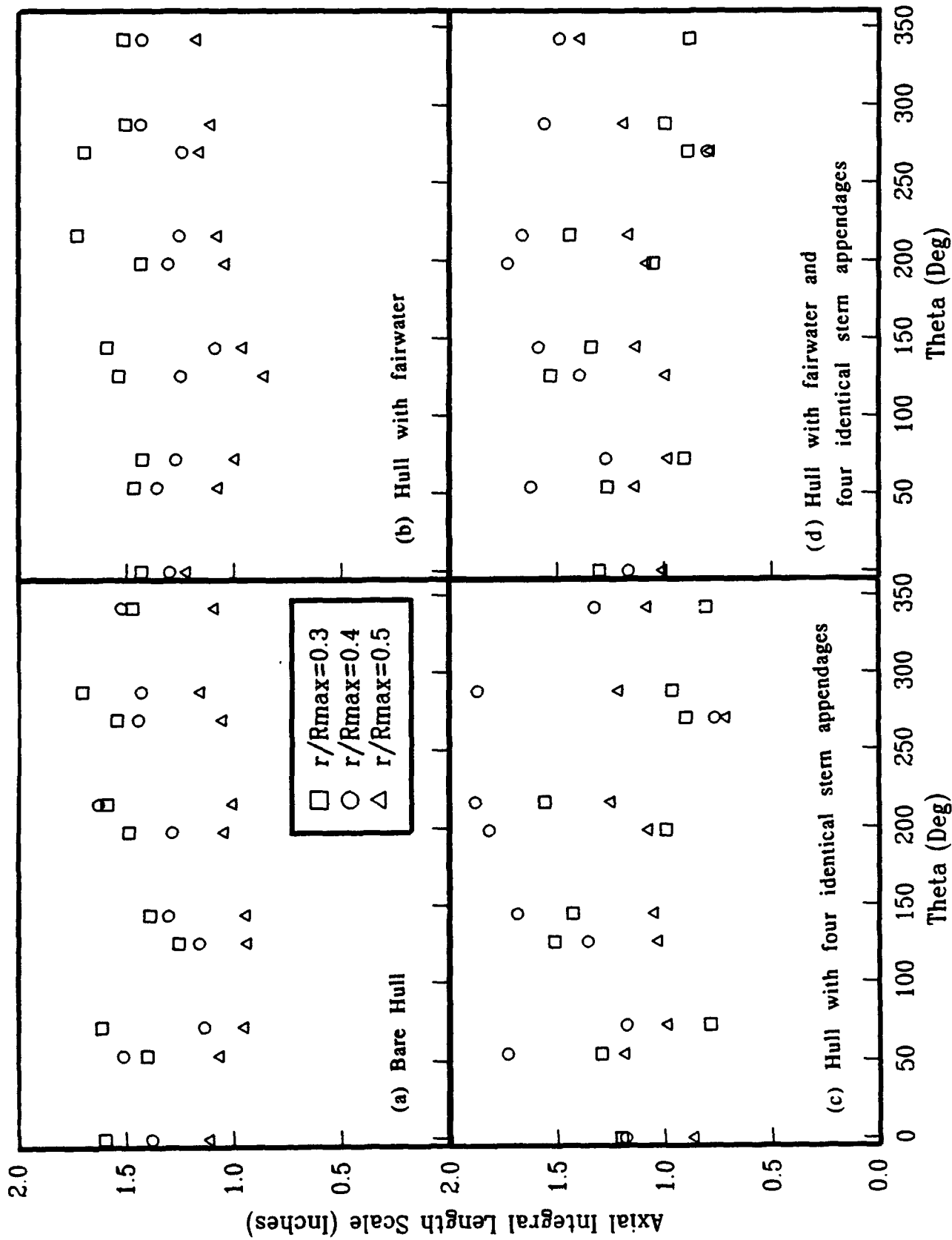


Fig. 8. Axial integral length scales Λ (inches) at $x/L=0.978$

derived from hot-wire measurements.

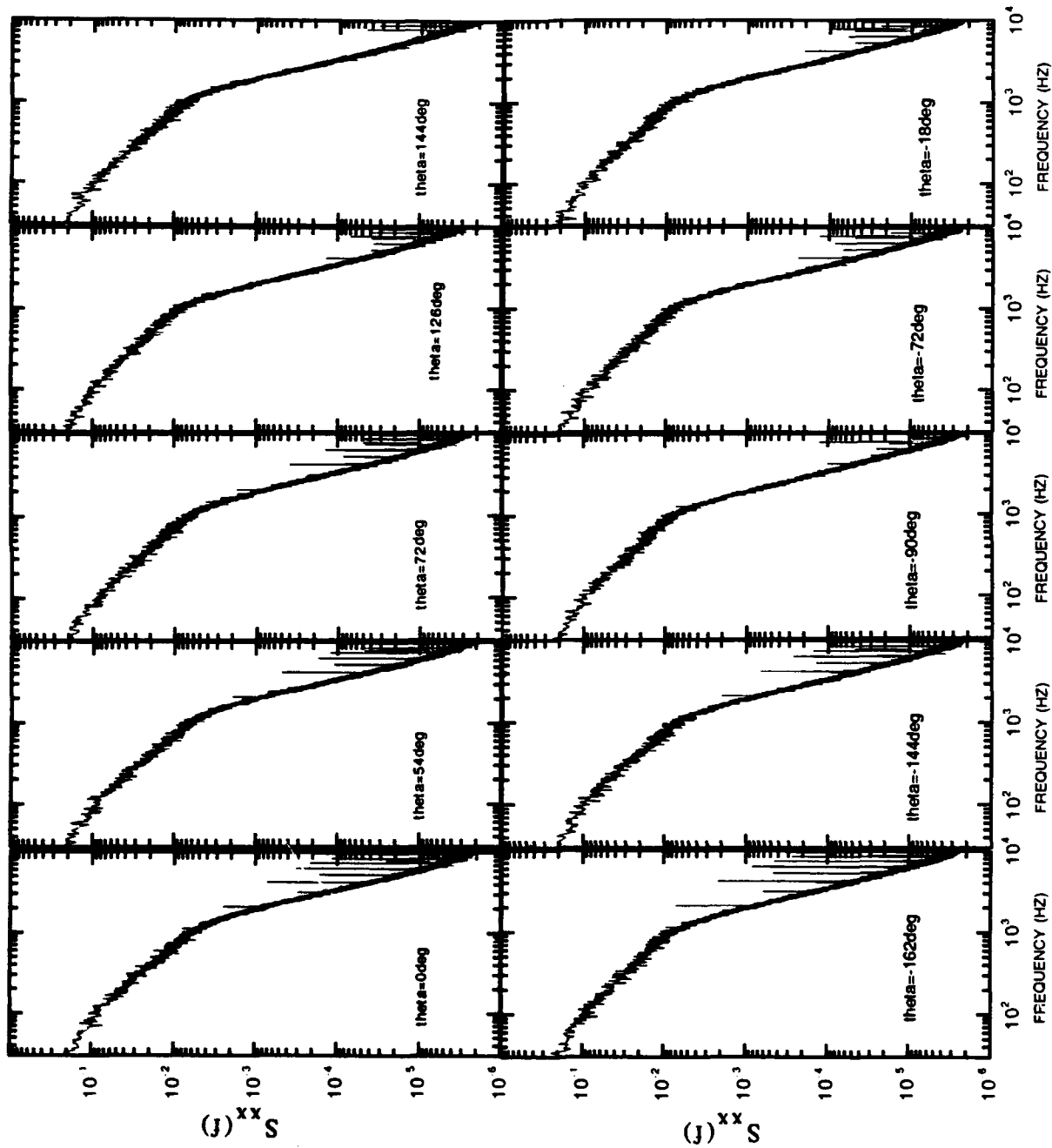


Fig. 9a. $r/R_{max}=0.3$.

Fig. 9. Spectral density function for bare hull at $x/L=0.978$ for ten angles and three radii.

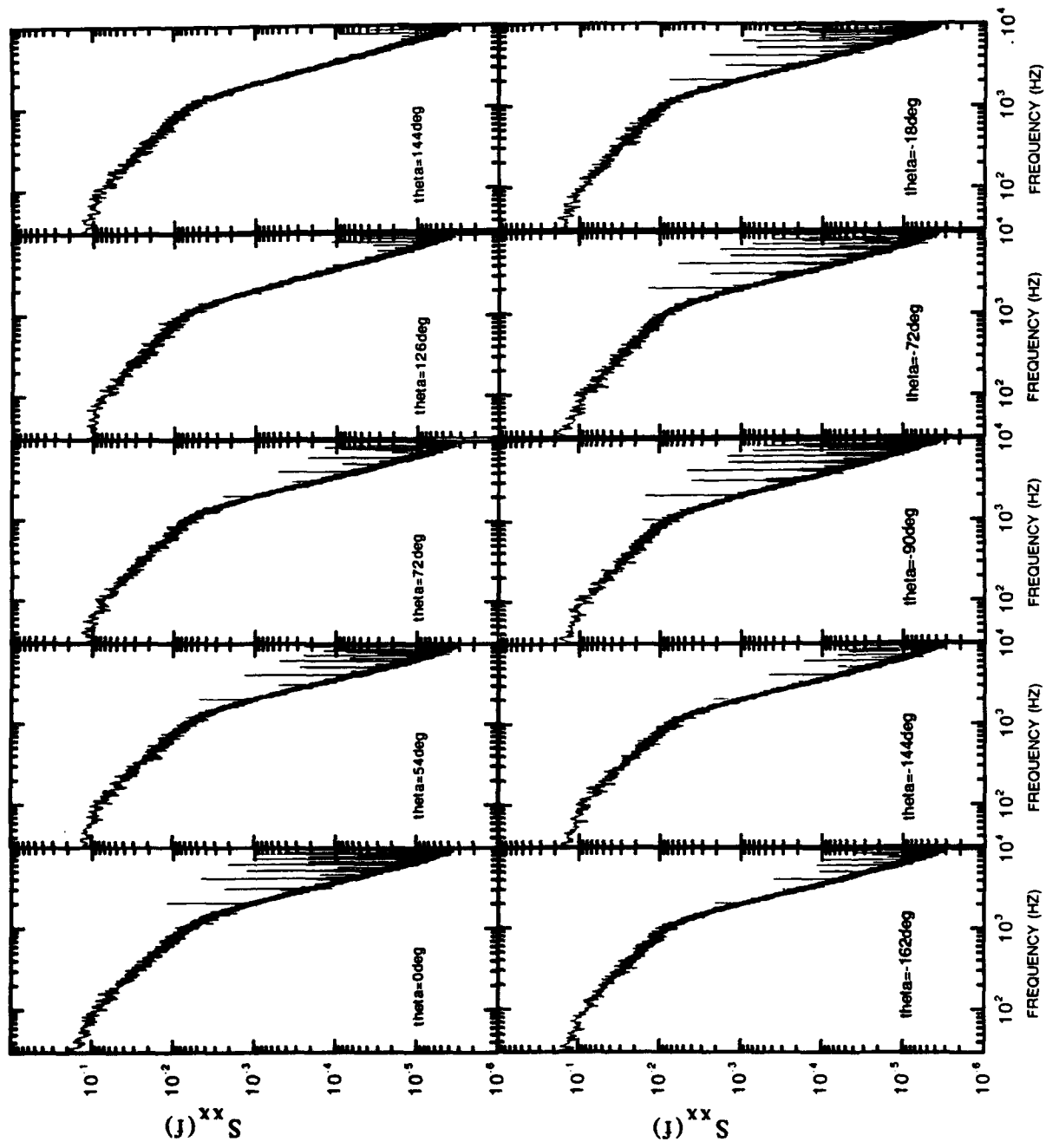


Fig. 9b. $r/R_{\max} = 0.4$.

Fig. 9. (Continued)

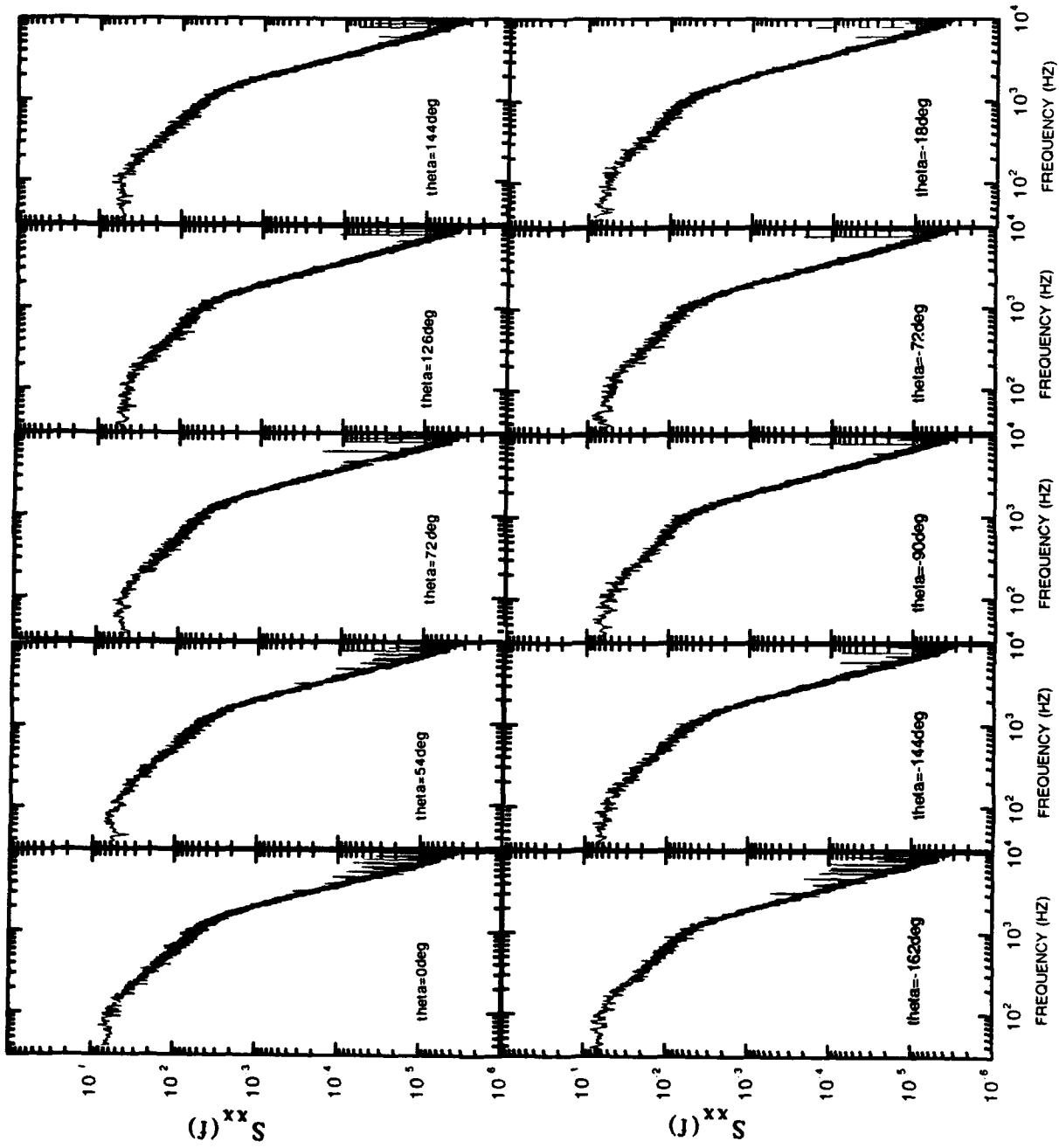


Fig. 9c. $r/R_{max}=0.5$.

Fig. 9. (Continued)

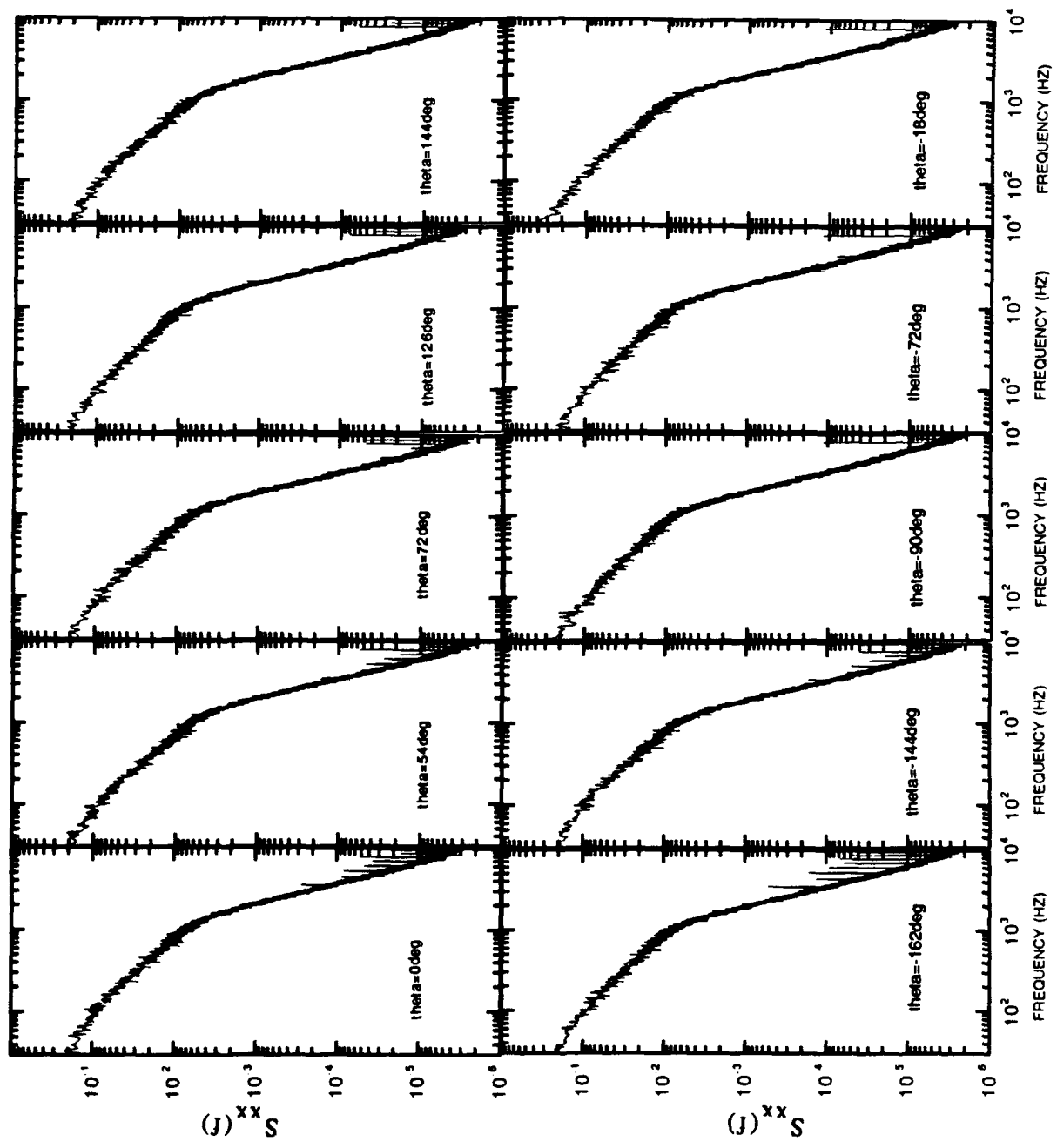


Fig. 10a. $r/R_{max}=0.3$.

Fig. 10. Spectral density function for hull with fairwater at $x/L=0.978$ for ten angles and three radii.

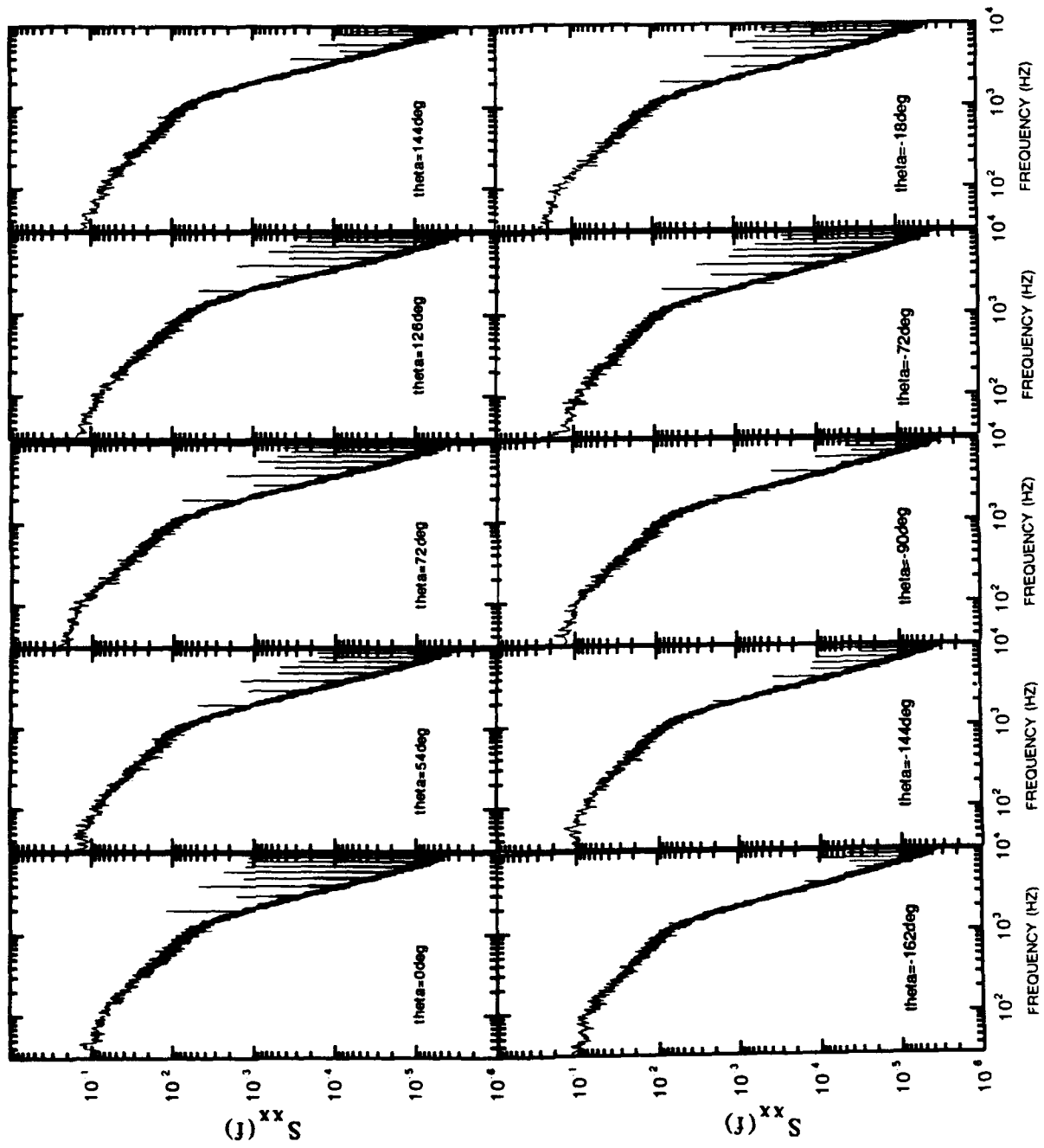


Fig. 10b. $r/R_{\max} = 0.4$.

Fig. 10. (Continued)

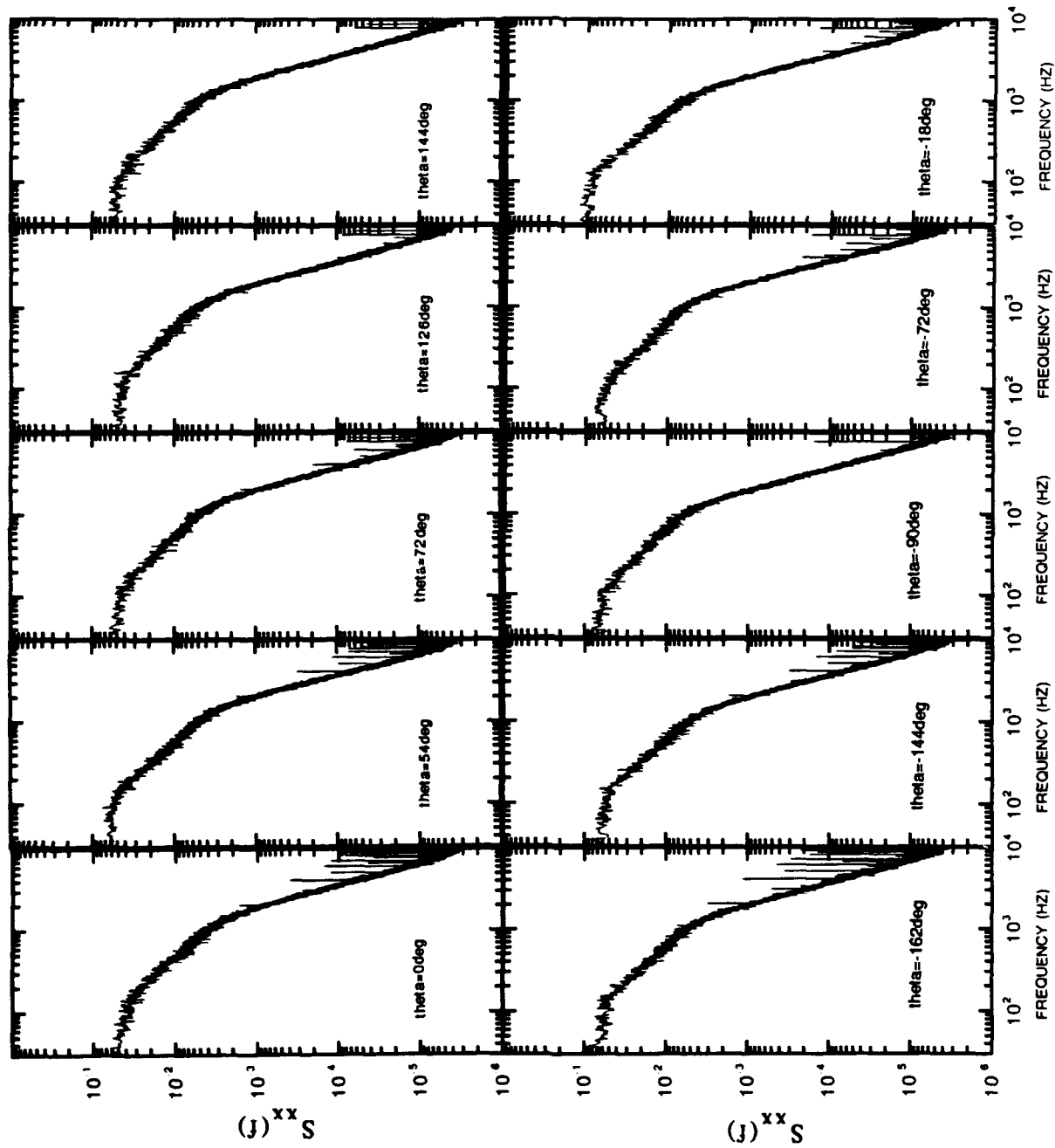


Fig. 10c. $r/R_{max}=0.5$.

Fig. 10. (Continued)

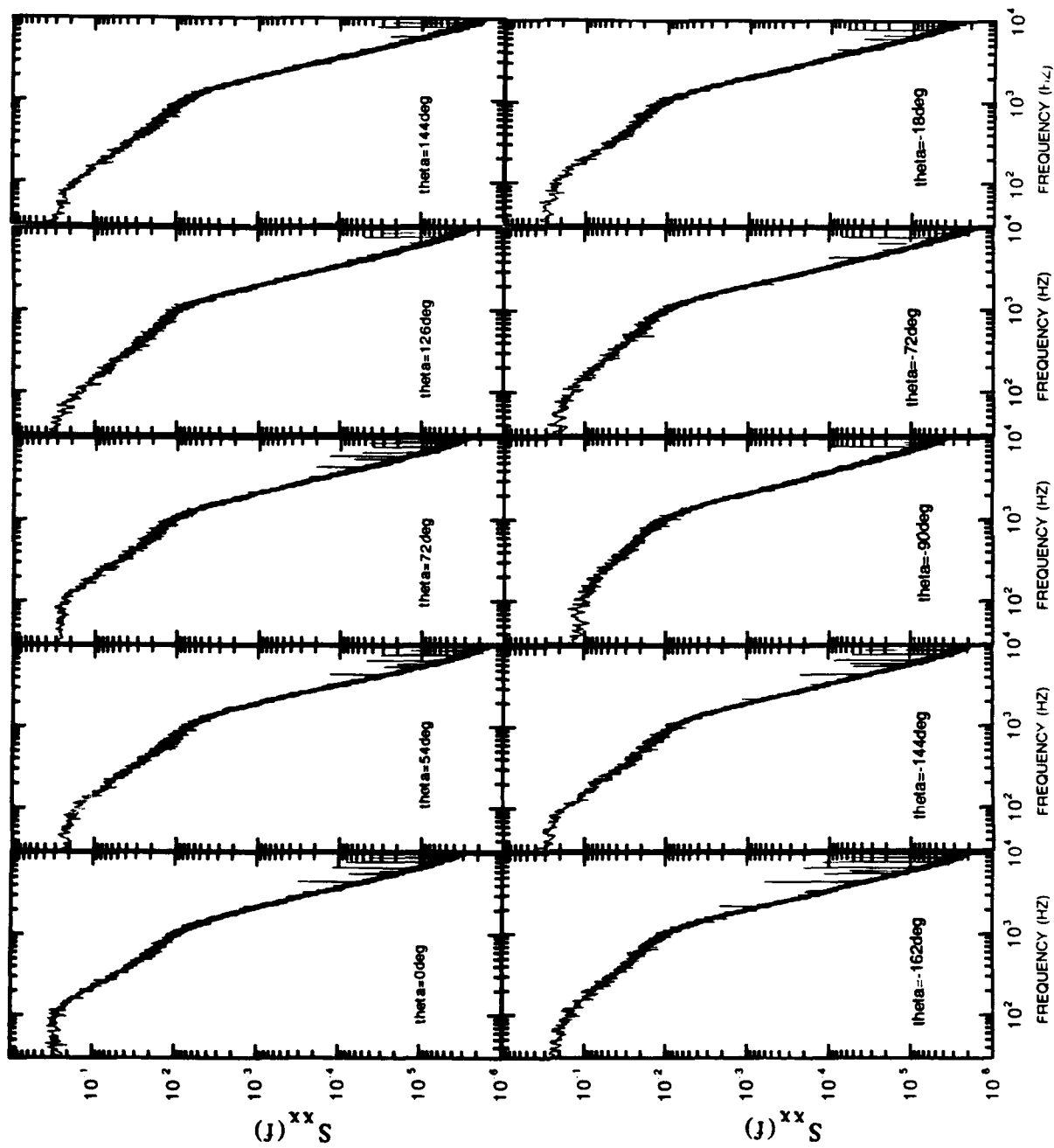


Fig. 11a. $r/R_{max}=0.3$.

Fig. 11. Spectral density function for hull with four identical stern appendages at $x/L=0.978$ for ten angles and three radii.

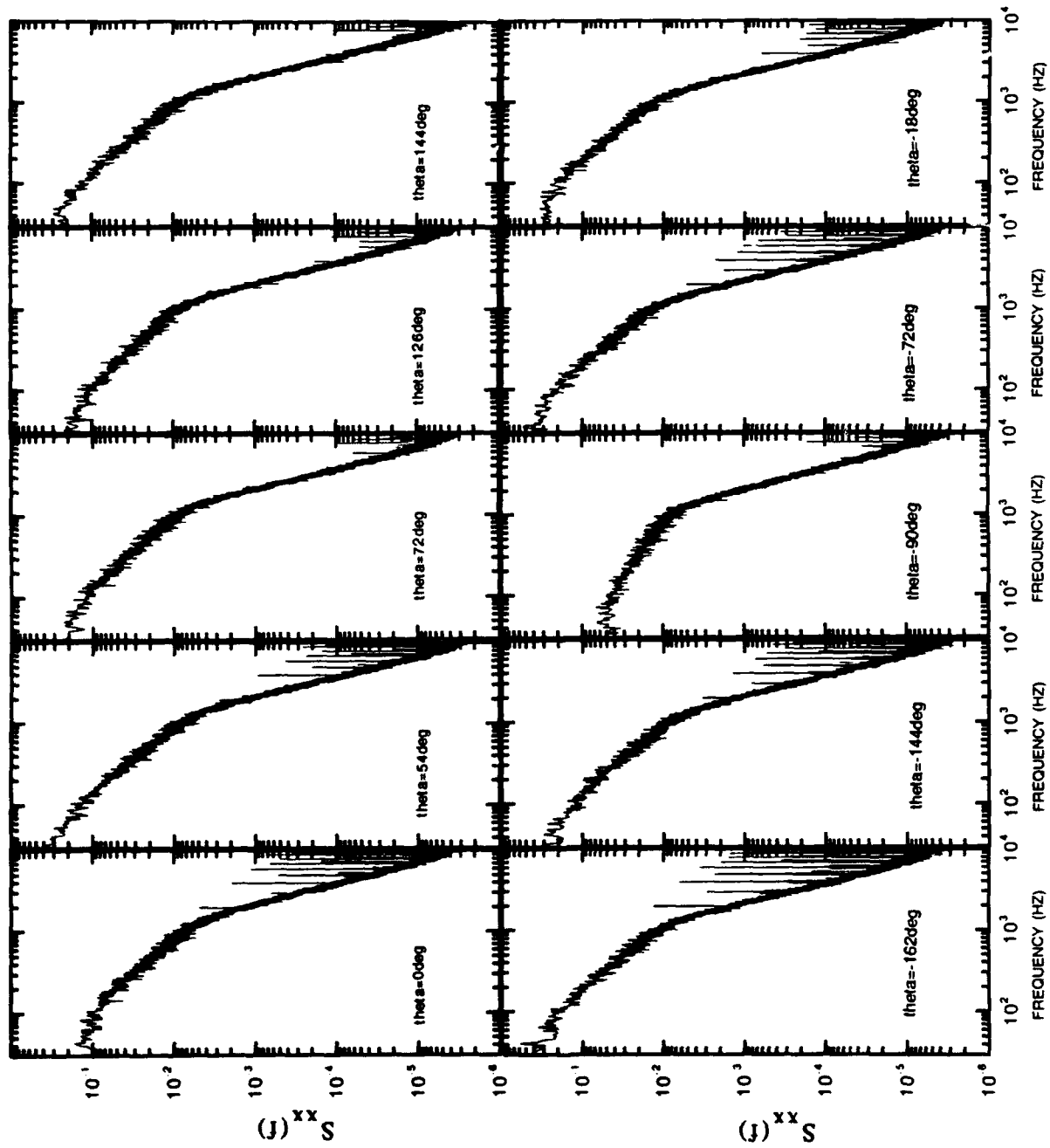


Fig. 11b. $r/R_{\max}=0.4$.

Fig. 11. (Continued)

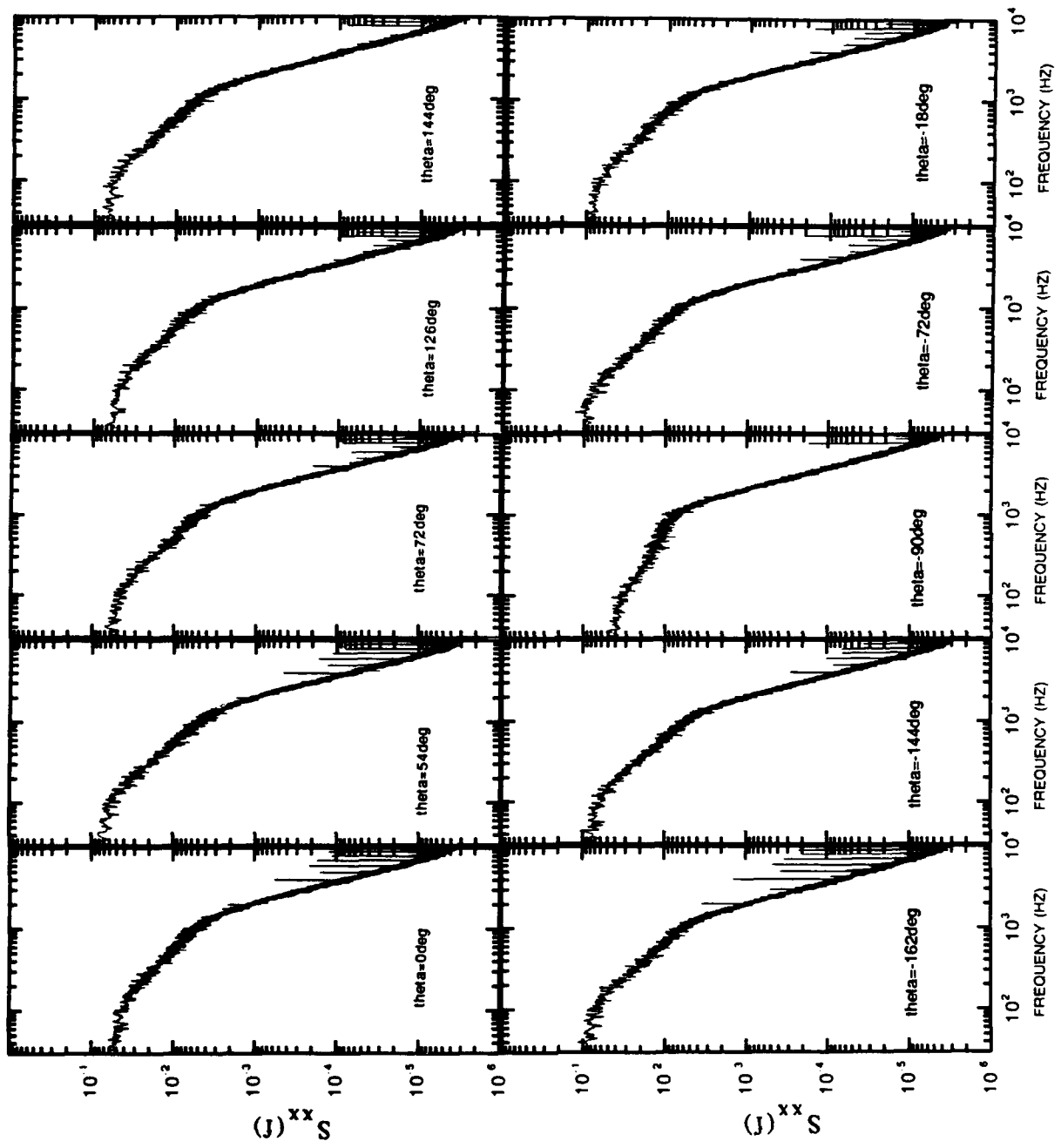


Fig. 11c. $r/R_{\max} = 0.5$.

Fig. 11. (Continued)

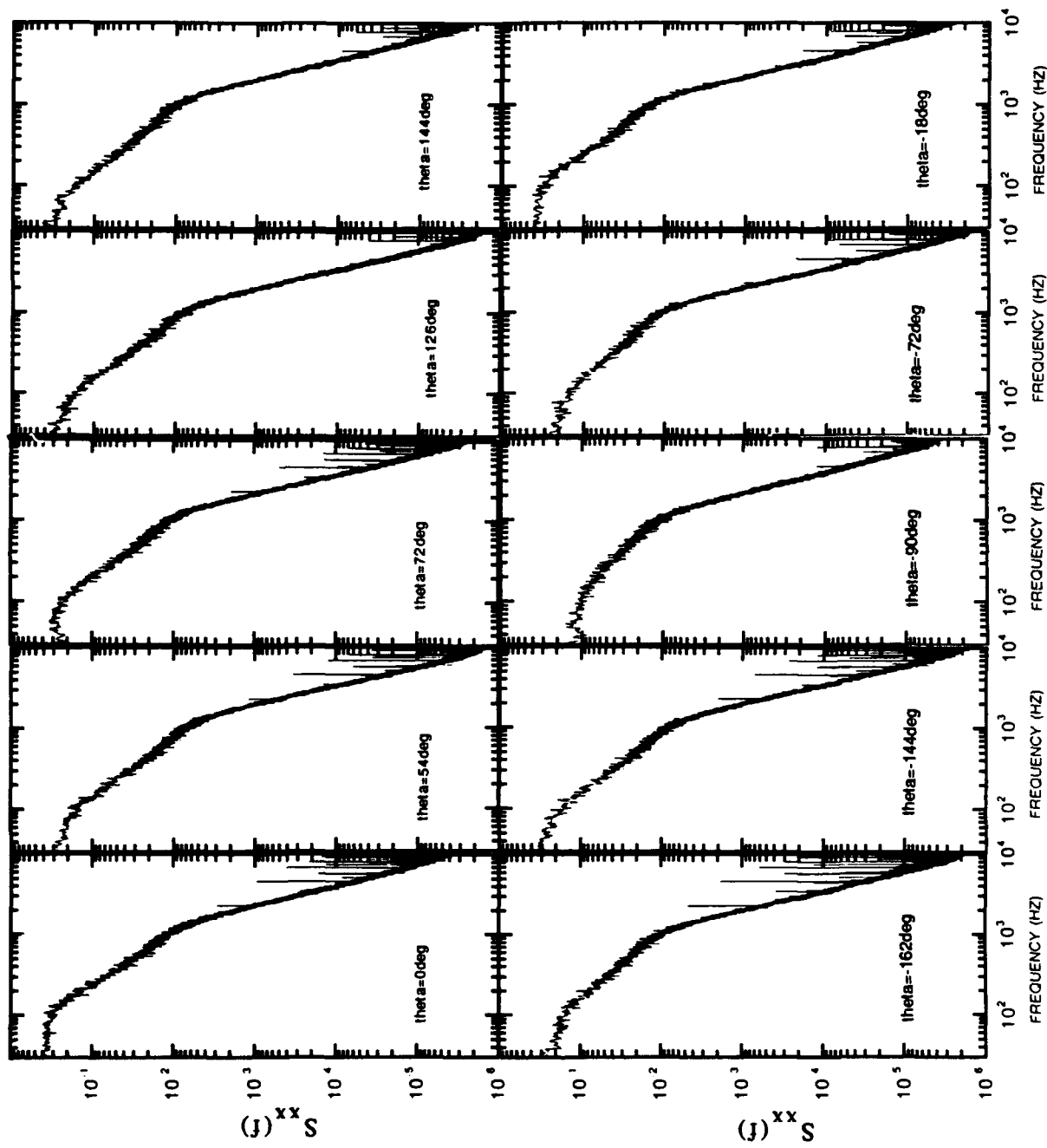


Fig. 12a. $r/R_{max}=0.3$.

Fig. 12. Spectral density function for hull with fairwater and four identical stern appendages at $x/L=0.978$ for ten angles and three radii.

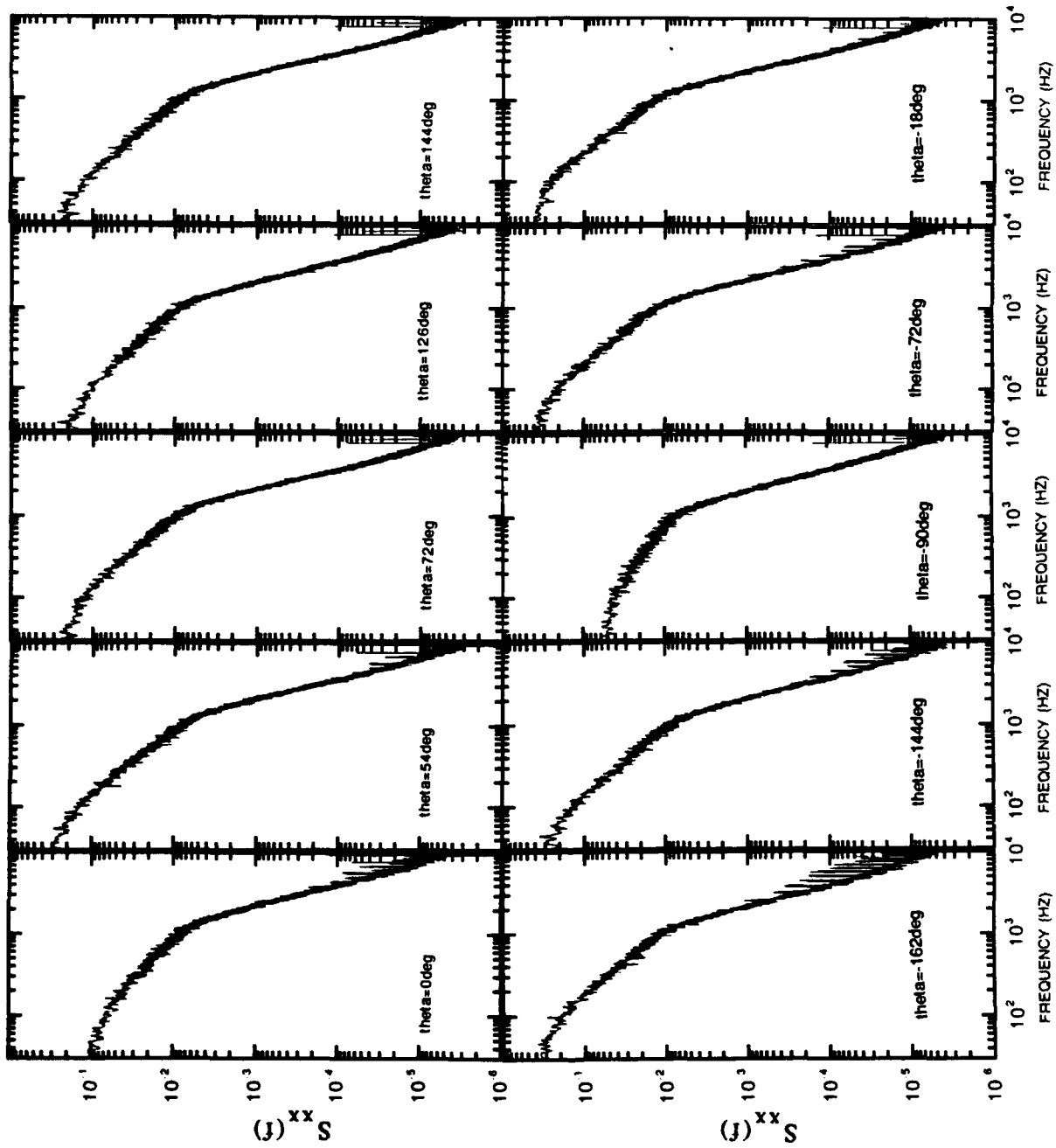


Fig. 12b. $r/R_{max}=0.4$.

Fig. 12. (Continued)

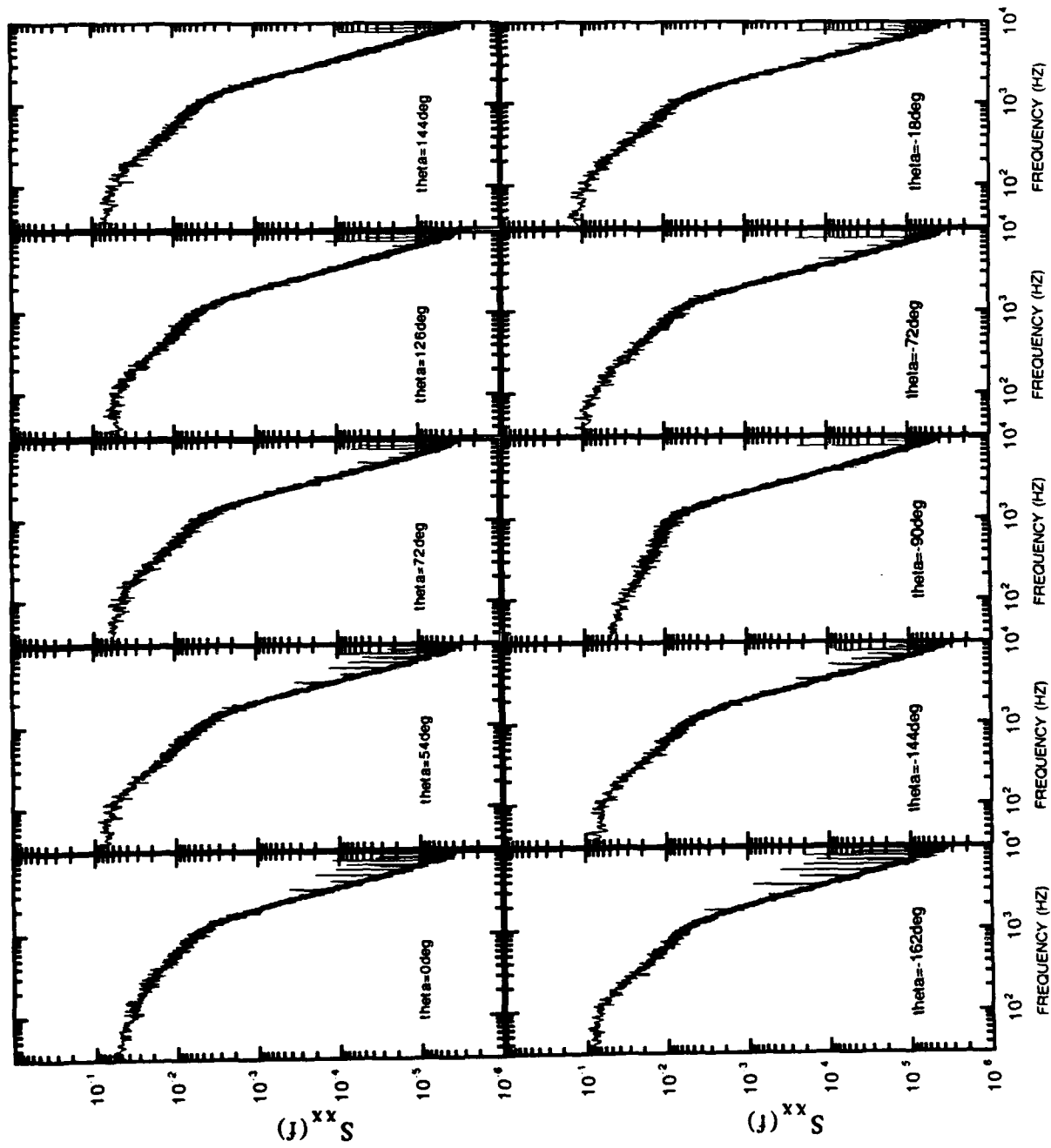


Fig. 12c. $r/R_{max}=0.5$.

Fig. 12. (Continued)

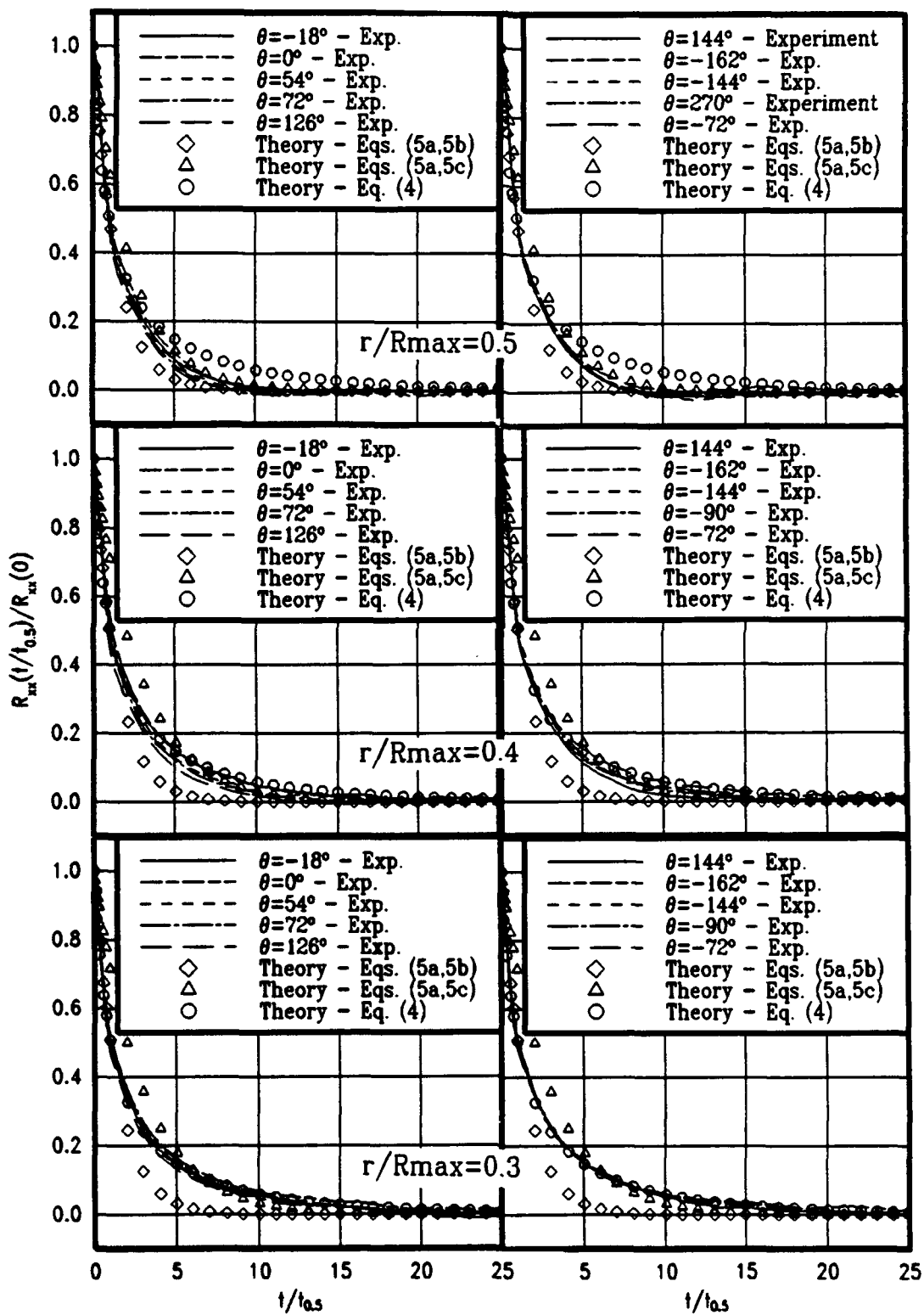


Fig. 13. Comparison of experimental and analytical correlation functions for bare hull at $x/L=0.978$

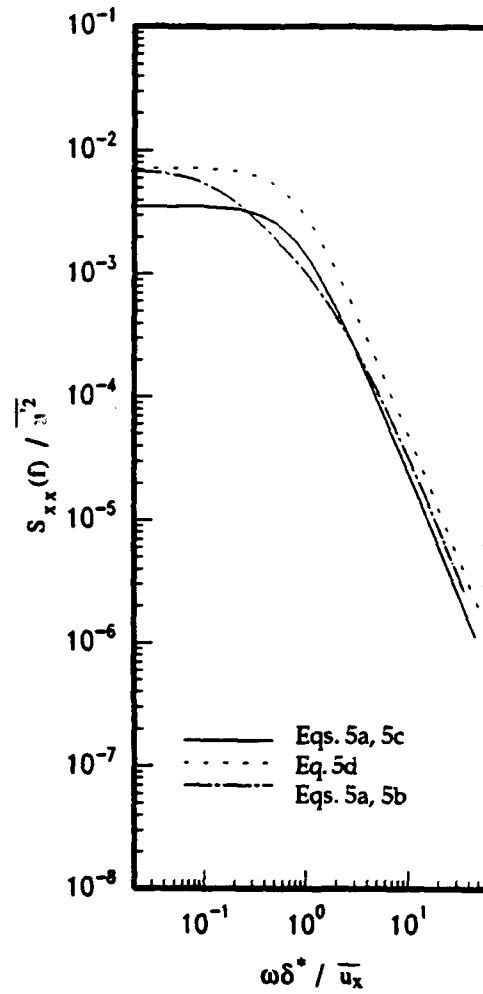


Fig. 14. Fourier transform of three analytical correlation functions.

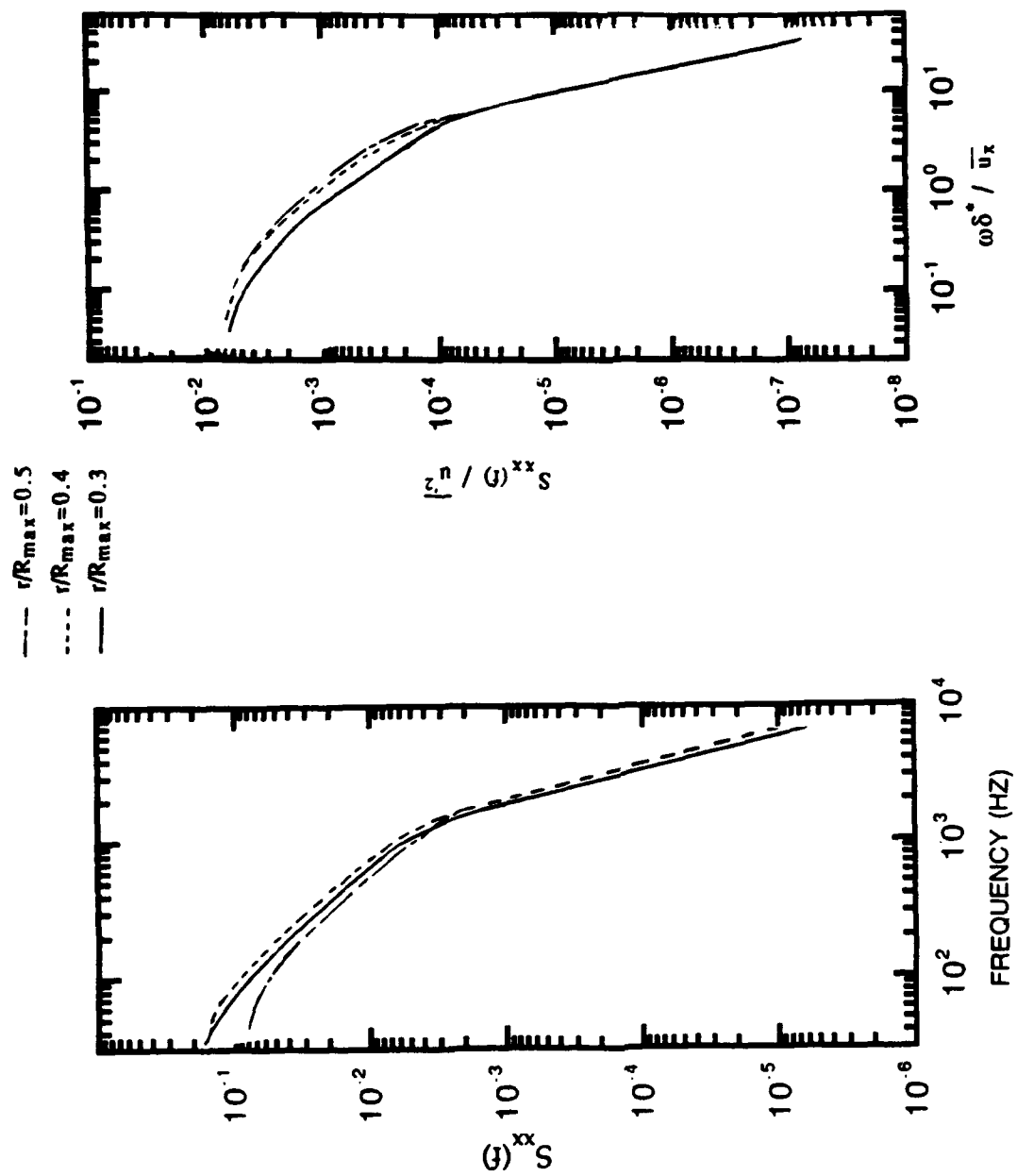


Fig. 15. Experimental turbulence spectrum at $x/L=0.978$ for bare hull at $\theta=0^\circ$.

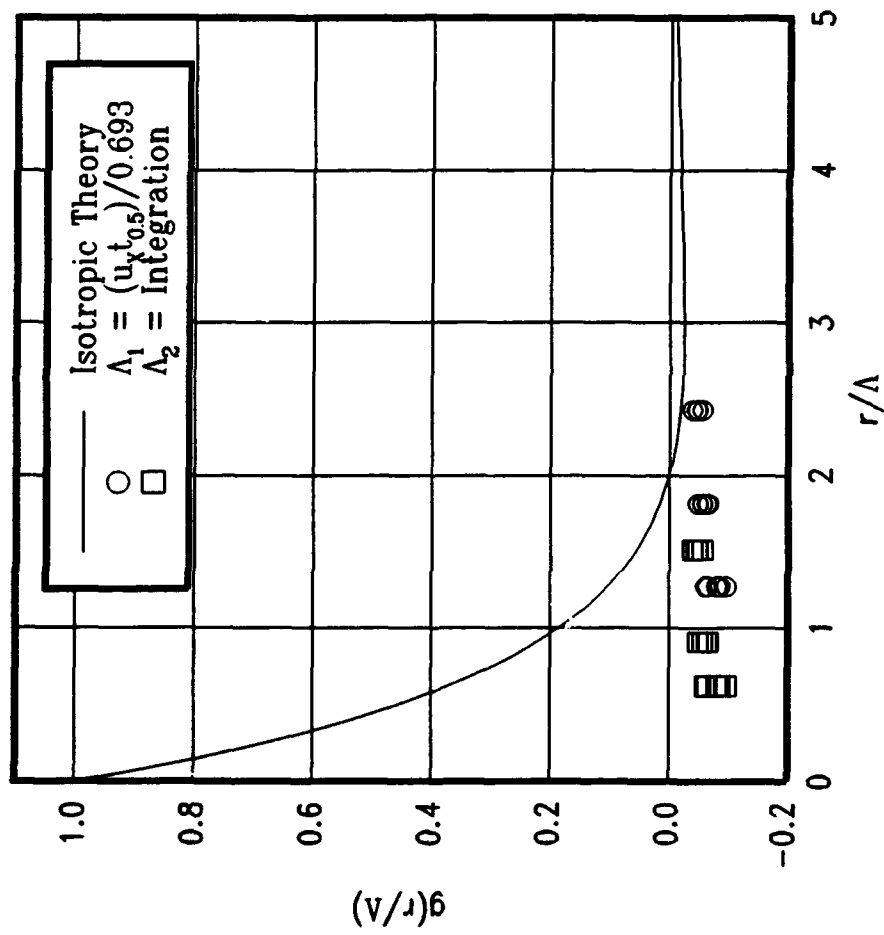


Fig. 16. Comparison of experimental and theoretical transverse correlation for bare hull at $x/L=0.978$.

REFERENCES

1. Sevik, M, "Sound Radiated from a Subsonic Rotor Subjected to Turbulence," Fluid Mechanics, Acoustics and Design of Turbomachinery: Part II, NASA SP-304, pp. 493-511 (1974).
2. Jiang, C.W., M.C. Chang, and Y. N. Liu, "The Effect of Turbulence Ingestion on Propeller Broadband Thrust," DTRC/SHD-1355-02 (Dec 1991).
3. Martinez, R. and K. Weissman, "Spatial-Domain Analysis of the Thrust on a Propeller Cutting Through Isotropic Turbulence," CAA Report U-1894-358.47 (1990).
4. Brooks, T. F. and R. H. Schlinker, "Progress in Rotor Broadband Noise Research," Vertica Vol. 7, No. 4, pp. 287-307 (1983).
5. Aravamudan, K. S. and W. L. Harris, "Low-Frequency Broadband Noise Generated by a Model Rotor," J. Acoust. Soc. Am. 66(2) (1979).
6. Humbad, N. G. and W. L. Harris, "Model Helicopter Rotor Low Frequency Broadband Noise," Vertica, Vol 6, pp. 19-35 (1982).
7. J. O. Hinze, Turbulence, McGraw-Hill, New York, (1959).
8. Huang, T.T., H.L Liu, and N.C. Groves, " Experiments of the DARPA SUBOFF Program," DTRC/SHD-1298-02 (Dec 1989).
9. Groves, N.C., T.T. Huang, and M.S. Chang, "Geometric Characteristics of DARPA SUBOFF Models," DTRC/SHD-1298-01 (Mar 1989).
10. Blanton, J. N., T. J. Forlini, and L. P. Purtell, "Hot-Film Velocity Measurement Uncertainty for DARPA SUBOFF Experiments," DTRC/SHD-1298-05 (Mar 1990).
11. Taylor, G.I., "The Spectrum of Turbulence," Proc. Roy. Soc. A, 164, 476 (1938).
12. Tennekes, H. and J. L. Lumley, A First Course in Turbulence, The MIT Press, Cambridge, Massachusetts, (1973).